Applied Thermal Engineering 270 (2025) 126153

Contents lists available at ScienceDirect

Applied Thermal Engineering

journal homepage: www.elsevier.com/locate/apthermeng

Research Paper

Topology optimization of microchannel heat sinks for laminar flows of thermal–fluid

Haitao Han [a], Yeming Han [b], Yu Lin [b], Chengmiao Wang [b], Jan G. Korvink [c,*], Yongbo Deng [c,*]

[a] School of Mechanical Engineering, Guizhou Institute of Technology, Guiyang 550003, China
[b] State Key Laboratory of Applied Optics, Changchun Institute of Optics, Fine Mechanics and Physics (CIOMP), Chinese Academy of Sciences, Changchun 130033, China
[c] Institute of Microstructure Technology (IMT), Karlsruhe Institute of Technology (KIT), Hermann-von-Helmholtzplatz 1, 76344 Eggenstein-Leopoldshafen, Germany

ARTICLE INFO

Keywords:
Topology optimization
Thermal–fluid coupling problem
Laminar flow
Microchannel
Heat sinks

ABSTRACT

In practical applications, the optimized design of microchannel heat exchangers is a result of a proper balance between thermal and hydraulic performances. This suggests that material properties and flow conditions determine the upper limit of the performance of microchannel heat exchangers. Exploring the influence of the material properties and flow conditions on the microchannel heat exchangers is beneficial for establishing more cost-effective solutions in the design process of microchannel heat exchangers, i.e., finding the optimal combination of materials, flow conditions, and microchannel structures. To explore the impact of physical conditions on the thermal performance of an optimized microchannel structure, this study innovatively proposes a single-objective topology optimization method constrained by relaxed fluid energy dissipation. The two-dimensional and three-dimensional topology optimization models were systematically analyzed. The numerical results indicate that the fluid energy dissipation constraint is equivalent to the pressure drop constraint. The performance of microchannel structures greatly varies with physical conditions and exhibits similar regularities in two-dimensional and three-dimensional cases. An increase in Reynolds number, an increase in Péclet numbers, a synergistic increase in both numbers, as well as an increase in solid–liquid heat conduction ratio can enhance thermal indicators. In two-dimensional problems, the maximum reductions in objective function are 79.37%, 44.4%, 98.54%, and 99.43%; whereas in three-dimensional problems, the values are 63.64%, 89.67%, 12.08%, and 99.43%, respectively. Based on similar regularities in both two-dimensional and three-dimensional cases, a strategy to improve efficiency of topology optimization design for three-dimensional microchannel heat exchangers is proposed.

1. Introduction

Advances in manufacturing technology, particularly in miniaturization and integration of transistors, have led to the development of electronic devices with higher power density and smaller size [1]. As a consequence, the heat flux generated by electronic chips now exceeds 100 W/cm^2 [2]. Due to the thermal–mechanical effects [3,4], accumulated heat directly affects the performance and lifespan of electronic devices. Therefore, addressing high-density heat flux is of great importance in industrial applications [5]. Microchannel heat sinks have gained widespread recognition as one of the most efficient approaches to address this challenge, mainly because of their high surface area-to-volume ratio and superior heat transfer coefficients compared to macrochannels [6]. Since their pioneering proposal by Tuckerman and Pease [7], microchannel heat sinks have been extensively explored for their immense potential in achieving high cooling efficiency [8,9].

In the past few decades, numerous novel channel structures have been proposed to enhance heat transfer. High-efficiency microchannel structures proposed through heuristic approaches include rectangular cross-section microchannels [10], wavy microchannels [11], microchannels with secondary structures [12], and microchannels with complex geometric features [13–15]. However, these designs heavily depend on the knowledge, experience, and intuition of designers and may not provide optimal solutions to certain problems. Therefore, design methodologies guided by optimization algorithms, including size and shape optimization [16] as well as surface property optimization [17,18], have been widely adopted to improve the thermal and hydraulic performance of channel structures. Nevertheless, these methods are limited by the initial channel structure and a lower degree of design

* Corresponding authors.
E-mail addresses: jan.korvink@kit.edu (J.G. Korvink), yongbo.deng@kit.edu (Y. Deng).

https://doi.org/10.1016/j.applthermaleng.2025.126153
Received 24 December 2024; Received in revised form 2 March 2025; Accepted 3 March 2025
Available online 7 March 2025

Nomenclature

Symbols

T_b	Ambient temperature
L	Characteristic length (m)
U	Characteristic length velocity (m/s)
V_c	Constraint value of the fluid volume fraction
ξ	Critical transformation point
J_{Fc}	Constraint value of J_F
$\tilde{\bar{\gamma}}$	Density variable
J_F	Dimensionless fluid dissipation power
$\overline{\nabla}$	Dimensionless gradient operator
$\bar{\alpha}$	Dimensionless inverse permeability
$\overline{T}_{TD}$	Dimensionless inlet temperature
$\bar{p}_{in}$	Dimensionless inlet pressure
$\overline{T}_{\max}$	Dimensionless maximum temperature
$\bar{p}_{out}$	Dimensionless outlet pressure
$\bar{p}$	Dimensionless pressure
$\bar{\sigma}$	Dimensionless stress tensor
$\overline{T}$	Dimensionless temperature
γ	Design variable
$\overline{\mathbf{u}}$	Dimensionless velocity vector
$\tilde{\gamma}$	Filtered variable
M_s	Finite-element mesh size
ρ	Fluid density (kg/m^3)
Ω_f	Fluid region
V	Fluid volume fraction
∇	Gradient operator (1/m)
Q_f	Heat source in fluid (W/m^3)
Q_s	Heat source in solid (W/m^3)
J_{th}	Objective function
$\mathbf{n}$	Out normal vector
pl	Penal factor
q	Penalization factor
β	Projection slope
Pe	Péclet number
Pr	Prandtl number
r	Radius of filter
Re	Reynolds number
C_p	Specific heat capacity of fluid (J/(kg·K))
Ω_s	Solid region
T	Temperature (K)
TO	Topology optimization
k_f	Thermal conductivity of fluid (W/(m·K))
k_s	Thermal conductivity of solid (W/(m·K))
k_r	k_s/k_f
T_n	The relative value of $\overline{T}_{\max}$
J_{Fn}	The relative value of J_F
J_n	The relative value of J_{th}
Δp	The relative value of dimensionless pressure drop
ΔT	The relative of maximum difference of $\overline{T}$
$\alpha_{\max}$	Value of $\bar{\alpha}$ in the solid region
$\mathbf{u}$	Velocity vector (m/s)

freedom, thus hindering the generation of innovative topological structures.

Topology optimization (TO) is a method of structural design driven by optimization; it is capable of producing an innovative optimal design with minimal reliance on the intuition and experience of the designer [19–21]. TO was initially introduced by Bendsøe and Kikuchi in 1988 for the purpose of designing mechanical structures that can withstand specified loads [22]. In 2003, Borrval and Petersson [23] first introduced the TO concept to Stokes flow. Later, Dede [24] and Yoon [25] employed two-dimensional (2D) TO to develop laminar flow heat dissipation structures in forced convection heat transfer systems. The key distinction between their TO models lies in the use of a multi-objective function by the former as opposed to a single-objective function used by the latter.

In recent years, TO has been increasingly used in thermal–fluid problems for microchannel heat sink design. Koga et al. [26] proposed a systematic development framework for the design of an optimized heat sink. Marck et al. [27] investigated bi-objective TO based on the finite-volume and discrete adjoint methods. Qian and Dede [28] proposed a continuous adjoint method. Liu et al. [29] proposed a multi-objective TO approach with three objective functions. Sato et al. [30] proposed an adaptive weighting scheme for bi-objective TO. Lv and Liu [31] explored the impact of four parameters on the bi-objective TO, specifically examining the Darcy number, Penalty factors, inlet velocity, and weighting ratio. Dong and Liu [32] and Subramaniam et al. [33] investigated the impact of weighting coefficient on the multi-objective TO. Zhang and Gao [34] investigated a TO method for non-Newtonian cooling fluids. Xia et al. [35] investigated the impact of inlet and outlet structure on the bi-objective TO. Wang et al. [36] analyzed the impact of the Reynolds number (Re) and dimensionless heat generation coefficient on a bi-objective TO. Mekki et al. [37] developed a TO approach based on a genetic algorithm. Wang et al. [38] proposed a multiobjective TO model based on the ε-constraint algorithm. Based on the moving morphable component (MMC) method, Zhao et al. [39] demonstrated a concurrent TO method of the channel, inlets, and outlets. Yu et al. [40] extended the MMCs to bi-objective TO based on a cubic order component with elliptic joints. Zeng and Lee [41] optimized a liquid-cooled microchannel heat sink fin, aiming to minimize pressure drop. Zou et al. [42] employed bi-objective TO for heat sink design in microelectronics. Qian et al. [43] used bi-objective TO to design a channel for the cold plate in a phased array antenna. Duan et al. [44] employed single-objective TO to design an air cooling structure for batteries. Li et al. [45] and Chen et al. [46] proposed a design for a liquid-cooled heat sink through a bi-objective TO. Wang et al. [47] proposed a plate heat exchanger by using single-objective TO. The aforementioned studies primarily focus on 2D thermal-fluid TO. The research involved includes algorithm development, objective function, interpolation function, and practical applications.

To balance computational efficiency and accuracy in approximating three-dimensional (3D) TO models, pseudo-3D TO methods have been developed. The approaches aim to reduce computational resources consumption while maintaining high precision. Pollini et al. [48] suggested a pseudo-3D model for a single-objective TO of natural convection problems. Ghasemi and Elham [49] proposed a pseudo-3D model for TO of pin–fin structure. Zhao et al. [50] proposed a pseudo-3D single-objective TO of planar cooling channels. Marinaro et al. [51] explored a pseudo-3D bi-objective TO of forced air-cooled heat sinks.

Research on 3D thermal-fluid coupled TO is significantly less extensive compared to its 2D counterpart. Sun et al. [52] proposed a method for large scale bi-objective TO and analyzed the influence of weighting coefficient. Rogié and Andreasen [53] demonstrated that 3D models offer significantly greater performance enhancement compared to pseudo-3D models. Zhang et al. [54] proposed a bi-objective level set TO method based on the radial basis functions. Dede [55] proposed a design of a multipass branching microchannel heat sink using bi-objective TO. Zhou et al. [56] and Gilmore et al. [57] proposed a manifold microchannel heat sink by using bi-objective TO. Yu et al. [58] proposed a design of cooling system in additively manufactured hot

stamping tools by using single-objective TO.

In summary, the majority of TO studies for liquid-cooled heat sinks have traditionally operated under the assumptions of laminar flow, 2D modeling, and incompressible fluid. These approaches are typically founded on the density method and incorporate the method of moving asymptotes optimization algorithm proposed by Svanberg (1987) [59,60] to improve both thermal and hydraulic performances. In the context of bi-objective TO, the focus of research has mainly been on the exploration of the Pareto frontier. Moreover, there has been a discussion on the impact of parameters such as Darcy number, penalty factors, and *Re* on the optimized results. In the context of single-objective TO, the maximization of heat dissipation while obeying constrains on fluid energy dissipation is crucial for practical applications. In the previous literatures, research on the single-objective TO problem was mainly focused on the realization and demonstration of the optimization design. Furthermore, those researches have indicated that the single-objective TO can yield optimized results.

However, in single-objective TO for microchannel heat sink, the choice of fluid or solid material and the flow conditions determine the performance of the optimized result. However, their impact on the optimized structure remains unknown. During the TO design process, parameter selection relies on empirical knowledge and iterative experimentation, which can be a time-intensive endeavor, particularly when addressing the 3D problem. In general, to improve computational efficiency, the 3D topology optimization problem is reduced to a 2D problem. However, there is much more performance enhancement to gain from the 3D topology optimization of heat sinks than what is described by the 2D models. It is essential to validate the correlation between the parameters of the 2D and 3D topology optimization to determine their most significant impact on the optimized structures. Thus, the influence of four parameters on the optimized results was investigated in this study.

To facilitate a clear and comprehensive discussion and comparison of the performance of the TO results under different parameters, an innovative approach has been adopted, utilizing the least-squares objective for temperature in the solid domain while imposing a loose equality constraint on fluid energy dissipation. We present the relative changes in the multiple indicators of the optimized structure, including the relative value of objective $J_n = J_{th}/\min\{J_{th}\}$, relative value of the maximum dimensionless temperature in the solid domain $T_n = \overline{T}_{\max}/\min\{\overline{T}_{\max}\}$, the relative value of the viscous dissipation of fluid $J_{Fn} = J_F/J_{Fc}$, the volume fraction of the fluid domain V, the relative value of the dimensionless pressure drop $\Delta p = (\overline{p}_{in} - \overline{p}_{out})/\max\{(\overline{p}_{in} - \overline{p}_{out})\}$, and the relative value of the maximum dimensionless temperature difference in the solid domain $\Delta T = \Delta\overline{T}/\max\{\Delta\overline{T}\}$. For the TO of microchannel heat sinks, the explicit predefinition of the inlets and outlets is a crucial aspect. Previous studies have mainly focused on the use of single narrow inlet and outlet. However, it has been found that the configuration of the inlet and outlet exerts substantial impact on the topology and performance of microchannel heat sinks. Therefore, the full inlet and outlet of the microchannel are arranged to facilitate uniform liquid flow within the microchannels, thereby achieving a uniform temperature distribution in the solid domains.

The remainder of this paper is structured as follows: the mathematical description of the TO problem for microchannel heat sinks is presented in Section 2. The numerical implementation of the TO method is discussed in Section 3. Numerical study on the 2D and 3D TO regarding the Reynolds number (*Re*), Péclet number (*Pe*), and thermal conductivity is presented in Section 4. The discussion is presented in Section 5. Finally, the paper is concluded in Section 6.

2. Topology optimization problem

The TO problem of microchannel heat sinks for convective heat transfer in incompressible laminar flows is described by using the material distribution method in this section.

2.1. Model of fluid flow

To enhance the computational efficiency and numerical stability of the TO model for the thermal–fluid interaction system, this study employed a common sequential analysis method. The majority of research in the field of TO for the micron-scale dimensions of microchannel heat sinks is based on the following assumptions: the fluid within the microchannel heat sinks is assumed to be incompressible, fully developed, laminar and in steady flow state. The viscous dissipation inside the flow is not accounted for in the energy balance equation, the material properties are considered to be independent of temperature, and the buoyancy effect inside the fluid is neglected. And the validity of the TO method has been demonstrated using experimental and numerical methods [41]. Therefore, the dimensionless Navier–Stokes equations can be used to describe the motion of a Newtonian fluid as

$$\begin{cases} \overline{\mathbf{u}}\cdot\overline{\nabla}\overline{\mathbf{u}} + \overline{\nabla}\cdot\left[\overline{p}\mathbf{I} - \dfrac{1}{Re}\left(\overline{\nabla}\overline{\mathbf{u}} + \overline{\nabla}\overline{\mathbf{u}}^{\mathrm{T}}\right)\right] = \overline{\mathbf{f}}, & \text{in } \Omega \\ \nabla\cdot\mathbf{u} = 0, & \text{in } \Omega \end{cases} \tag{1}$$

where $\overline{\nabla} = L\nabla$ is the dimensionless gradient; L is the characteristic length; $\overline{\mathbf{u}} = \mathbf{u}/\mathrm{U}$; the dimensionless velocity vector; $\mathbf{u}$ is the velocity vector; U is the characteristic velocity of the fluid;$\overline{p} = p/\rho U^2$ is the dimensionless pressure; p is the pressure; ρ is the fluid density; $Re = \rho UL/\mu$ is the Reynolds number; μ is the dynamic viscosity of the fluid; $\overline{\mathbf{f}}$ is the dimensionless body force; and Ω is the design domain.

Based on the porous medium model [23], the dimensionless body force is the friction force expressed as

$$\overline{\mathbf{f}} = -\overline{\alpha}\overline{\mathbf{u}}, \quad \text{in } \Omega \tag{2}$$

where $\overline{\alpha}$ is the dimensionless inverse permeability of the porous medium. When the porosity of the porous medium is zero, it corresponds to a solid material with infinite impermeability and zero fluidic velocity achieved by the infinite friction force. When the porosity is infinite, it corresponds to the structural void for the transport of the fluid with zero impermeability. Thus, the impermeability of the porous medium model can be described as

$$\begin{cases} \overline{\alpha} = \alpha_{\max} \gg 0, & \text{in } \Omega_s \\ \overline{\alpha} = 0, & \text{in } \Omega_f \end{cases} \tag{3}$$

where Ω_s and Ω_f are the subdomains of solid and fluid in the design domain, respectively.

In TO, the density variable is used to interpolate the impermeability in the design domain as [50]:

$$\overline{\alpha}(\overline{\overline{\gamma}}) = \alpha_{\min} + \alpha_{\max}\left[1 - \frac{\overline{\overline{\gamma}}(1+q)}{q+\overline{\overline{\gamma}}}\right], \text{ in } \Omega \tag{4}$$

where $\overline{\overline{\gamma}}$ is the density variable; $\alpha_{\max}$ and $\alpha_{\min}$ are the impermeability of the solid and fluid phases, respectively; and q is the penalization factor used to tune the convexity of this interpolation, and it is chosen as 0.1 based on numerical tests. For the fluid phase, the impermeability is zero, i.e., $\alpha_{\min} = 0$. For the solid phase,$\alpha_{\max}$ should be theoretically infinite; numerically, it is chosen as the finite value of 10^6 to ensure the stability of the numerical implementation and approximate the solid phase with acceptable accuracy.

The density variable is obtained by sequentially implementing the filtering and projection operations on the design variable. The filtering is achieved by using a PDE filter to prevent the checkerboard and alleviate mesh dependency [61]. The PDE filter blurs the boundary between fluid and solid, creating a gray area. A threshold projection is applied to the filtered design variable to remove the gray area.

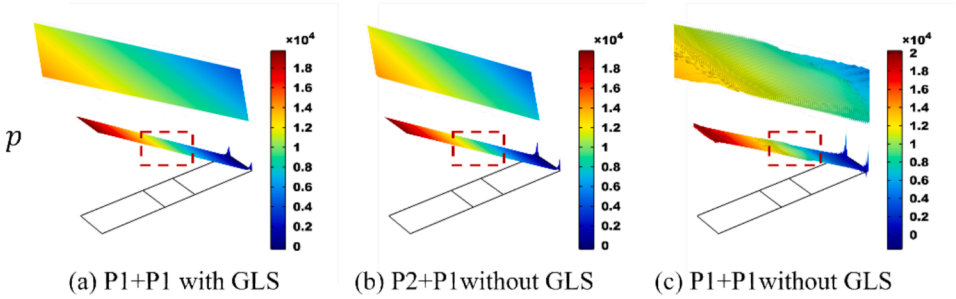

Fig. 1. Numerical solutions of pressure for the NS equations. (a) P1 for both velocity and pressure with GLS stabilization. (b) P2 for velocity and P1 for pressure. (c) P1 for both velocity and pressure.

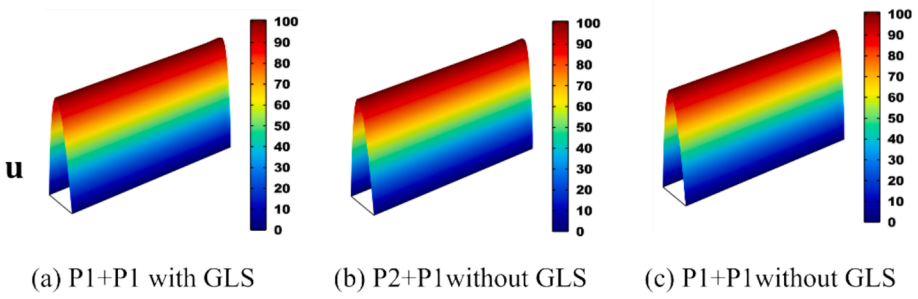

Fig. 2. Numerical solutions of velocity for the NS equations. (a) P1 for both velocity and pressure with GLS stabilization. (b) P2 for velocity and P1 for pressure. (c) P1 for both velocity and pressure.

2.2. Model of convective heat transfer

A uniformly distributed heat source is assumed within the solid domain. Thus, the steady-state energy equations in the fluid and solid domains are described as

$$\rho C_p \mathbf{u}\cdot\nabla T + \nabla\cdot\left(-k_f\nabla T\right) = 0, \quad \text{in } \Omega_f \tag{5}$$

$$\nabla\cdot(-k_s\nabla T) - Q_s = 0, \quad \text{in } \Omega_s \tag{6}$$

where C_p is the specific heat capacity of the fluid; T is the temperature; k_f is the thermal conductivity of the fluid; k_s is the thermal conductivity in the solid subdomain and Q_s, the power of the heat source in the solid subdomain.

In TO, the distribution of the fluid and the solid domains can be determined after the optimization. Therefore, one cannot know a priori which equation should be adopted at each point in design domain Ω. Therefore, Eqs. (5) and (6) are unified by introducing the density variable representing the distribution of the fluid and solid phases in the design domain. The dimensionless form is

$$\bar{\bar{\gamma}}^{2p} RePr(\overline{\mathbf{u}}\cdot\overline{\nabla}\overline{T}) + \overline{\nabla}\cdot(-\overline{k}(\bar{\bar{\gamma}})\overline{\nabla}\overline{T}) - \overline{Q}(\bar{\bar{\gamma}}) = 0, \quad \text{in } \Omega \tag{7}$$

where the dimensionless parameters are expressed as

$$\begin{cases} Pr = \dfrac{\mu C_p}{k_f} \\ \overline{T} = \dfrac{T - T_{in}}{T_b - T_{in}} \\ \overline{k}(\bar{\bar{\gamma}}) = 1 + (k_r - 1)(1 - \bar{\bar{\gamma}})^{pl} \\ \overline{Q}(\bar{\bar{\gamma}}) = \dfrac{L^2 Q_s}{(T_b - T_{in})k_f}\left(1 - \bar{\gamma}^{pl}\right) \end{cases}; \tag{8}$$

Pr is the Prandtl number; T_{in} is the fluid temperature at the inlet; $\overline{T}$ is the dimensionless temperature; $\overline{k}(\bar{\bar{\gamma}})$ is the interpolated dimensionless counterpart of the thermal conductivity; $k_r = k_s/k_f$ is the ratio of solid-to-fluid thermal conductivity; and $\overline{Q}(\bar{\bar{\gamma}})$ is the dimensionless counterpart of the interpolated heat source; and pl is the penal factor, with the value of 3. Eq. (7) can also be rewritten as

$$\bar{\bar{\gamma}}^{2p} Pe(\overline{\mathbf{u}}\cdot\overline{\nabla}\overline{T}) + \overline{\nabla}\cdot(-\overline{k}(\bar{\bar{\gamma}})\overline{\nabla}\overline{T}) - \overline{Q}(\bar{\bar{\gamma}}) = 0, \quad \text{in } \Omega \tag{9}$$

where $Pe = \rho C_P UL/k_f$ is the Péclet number.

2.3. Topology optimization model

Because uniform temperature distribution can enhance the stability and life of high-power microelectronic devices, the optimization objective is to achieve low and uniform temperature distribution in the solid domain. Therefore, the objective is defined as the least-squares objective for temperature in the solid domain:

$$J_{th} = \int_{\Omega}(1 - \bar{\bar{\gamma}})\overline{T}^2 d\Omega \tag{10}$$

where J_{th} denotes the optimization objective. The optimization objective is constrained by the fluid energy dissipation. The dimensionless total energy dissipation in the design domain can be expressed as

$$J_F = \int_{\Gamma_{in}\cup\Gamma_{out}}\left(\overline{p} + \frac{1}{2}\overline{\mathbf{u}}^2\right)(-\overline{\mathbf{u}}\cdot\mathbf{n})d\Gamma. \tag{11}$$

The objective function tends to drive the optimization result toward a structure entirely filled with fluid, which represents a poor local optimum and clearly lies outside the feasible design space. This is because the cooling efficiency of microchannels is primarily enhanced by increasing the fluid–solid contact area, and an all-fluid structure fails to provide the necessary solid support for practical applications. To ensure that the topology optimization results remain within the feasible design space, the volume constraint is employed to regularize the optimization problem and avoid such unrealistic solutions. When conducting a comparison of TO results, the volume constraint is imposed as equality constraint to facilitate a rigorous evaluation. However, equality constraints are often overly strict. This rigidity may lead to a significantly

reduced feasible solution space, potentially resulting in an empty set of viable solutions. Therefore, a volume constraint is imposed with a permissible relative tolerance of 10^{-3} based on the example test.

Based on the introduction of the Naiver–Stokes equations, porous medium model, convective heat transfer equation, and material interpolation, the TO problem for microchannel heat sinks can be formulated as

$$\min:\ J_{th}=\int_{\Omega}(1-\widetilde{\overline{\gamma}})\overline{T}^{2}d\Omega$$

$$s.t.\begin{cases}\begin{cases}\widetilde{\overline{\gamma}}^{p}\overline{\mathbf{u}}\cdot\overline{\nabla}\overline{\mathbf{u}}+\overline{\nabla}\cdot\left[\overline{p}\mathbf{I}-\dfrac{1}{Re}(\overline{\nabla}\overline{\mathbf{u}}+\overline{\mathbf{u}}\overline{\nabla})\right]+\overline{\alpha}(\widetilde{\overline{\gamma}})\overline{\mathbf{u}}=0\ \text{in}\Omega\\ \nabla\cdot\mathbf{u}=0\ \text{in}\Omega\\ \mathbf{n}\cdot\left[\overline{p}\mathbf{I}-\dfrac{1}{Re}(\overline{\nabla}\overline{\mathbf{u}}+\overline{\mathbf{u}}\overline{\nabla})\right]=\overline{\mathbf{g}}_{f}\ \text{on}\Gamma_{FN}\\ \overline{\mathbf{u}}=\overline{\mathbf{u}}_{D}\ \text{on}\Gamma_{FD}\end{cases}\\ \begin{cases}\widetilde{\overline{\gamma}}^{2p}Pe(\overline{\mathbf{u}}\cdot\overline{\nabla T})+\overline{\nabla}\cdot(-\overline{k}(\widetilde{\overline{\gamma}})\overline{\nabla T})-\overline{Q}(\widetilde{\overline{\gamma}})=0\ \text{in}\Omega\\ \mathbf{n}\cdot(-\overline{k}(\widetilde{\overline{\gamma}})\overline{\nabla T})=g_{TN}\ \text{on}\Gamma_{TN}\\ \overline{T}=\overline{T}_{TD}\ \text{on}\Gamma_{TD}\end{cases}\\ \begin{cases}-r^{2}\nabla^{2}\widetilde{\gamma}+\widetilde{\gamma}=\gamma\ \text{in}\Omega\\ \mathbf{n}\cdot\left(-r^{2}\nabla\widetilde{\gamma}\right)=0\ \text{on}\partial\Omega\end{cases}\ \text{(PDE filter)}\\ \left|\int_{\Omega}\widetilde{\overline{\gamma}}d\Omega/\int_{\Omega}1d\Omega-V_{c}\right|\le 10^{-3}\ \text{(Volume constraint)}\\ \widetilde{\overline{\gamma}}=\dfrac{\tanh(\beta\xi)+\tanh(\beta(\widetilde{\gamma}-\xi))}{\tanh(\beta\xi)+\tanh(\beta(1-\xi))}\ \text{(Threshold projection)}\\ |J_{F}-J_{Fc}|\le 10^{-3}\ \text{(Dissipation power constraint)}\end{cases}\tag{12}$$

where $\mathbf{n}$ is the outer normal vector of the boundary $\partial\Omega$ of the design domain; $\overline{\mathbf{g}}_f$ is the known stress distribution on the outlet boundary Γ_{FN}; g_{TN} is the known heat flux distribution on the outlet boundary Γ_{TN}; r is the radius of the PDE filter; $\widetilde{\gamma}$ is the filtered design variable; γ is the design variable. Based on the numerical test, $\xi\in[0,1]$ denotes the critical transformation point and β denotes the projection slope, which should be increased from one to a large number to ensure numerical stability. In the numerical implementation, ξ is set as 0.5; the initial value of β is 1, which is doubled at the 40th iteration and then doubled every 20 iterations until it reaches 2^{10}; V_c denotes the fluid volume.

To enhance the computational efficiency, the Navier–Stokes (NS) and convective heat transfer (CHT) equations are solved by using the Galerkin method based on the first-order finite elements. The GLS stabilization method is employed for both the NS equations and CHT equation. Supplementary stabilization terms are introduced into the weak formulations [62].

Suppose $\mathscr{S}$ and $\mathscr{C}$ are the appropriate trial solution spaces containing the approximating functions for the velocity and the pressure, respectively, and $\mathscr{V}$ and $\mathscr{C}$ are the test function spaces for velocity and pressure, respectively. The weak form of the NS equations is obtained as follows: find $(\overline{\mathbf{u}},\overline{p})\in\mathscr{S}\times\mathscr{C}$, such that $\forall(\overline{\mathbf{w}},\overline{q})\in\mathscr{V}\times\mathscr{C}$

$$\begin{aligned}\mathscr{W}_{up}(\overline{\mathbf{w}},\overline{q})=&\int_{\Omega}(\widetilde{\overline{\gamma}}^{p}\overline{\mathbf{u}}\cdot\overline{\nabla}\overline{\mathbf{u}}-\overline{\mathbf{f}})\cdot\overline{\mathbf{w}}+\overline{\sigma}:\overline{\nabla}\overline{\mathbf{w}}d\Omega+\int_{\Gamma_{FN}}-\overline{\mathbf{g}}_{f}\cdot\overline{\mathbf{w}}d\Gamma\\&+\int_{\Omega}-\overline{q}\nabla\cdot\mathbf{u}d\Omega-\sum_{e=1}^{n_{el}}\int_{\Omega^{e}}\tau_{PSPG}\overline{\nabla}\overline{q}\cdot\mathscr{R}(\overline{\mathbf{u}},\overline{p})d\Omega=0,\\&\forall(\overline{\mathbf{w}},\overline{q})\in\mathscr{V}\times\mathscr{C}\end{aligned}\tag{13}$$

where $\overline{\sigma}=\left[-\overline{p}\mathbf{I}+\frac{1}{Re}(\overline{\nabla}\overline{\mathbf{u}}+\overline{\mathbf{u}}\overline{\nabla})\right]$ denotes the dimensionless stress tensor; $\mathscr{R}(\overline{\mathbf{u}},\overline{p})=\widetilde{\overline{\gamma}}^{p}\overline{\mathbf{u}}\cdot\overline{\nabla}\overline{\mathbf{u}}-\overline{\sigma}-\overline{\mathbf{f}}$ is the residual; and τ_{PSPG} is the stabilization parameter for the pressure-stabilizing term, which is chosen as $\tau_{PSPG}=h_e^2Re/12$ with h_e and n_{el} representing the local element size and the number of the finite elements used to discretize Ω, respectively.

The effectiveness of the GLS stabilization form for the NS equations is illustrated in Figs. 1 and 2. In Fig. 1(a) and Fig. 2(a), first-order elements (P1) are used for both velocity and pressure with GLS stabilization. Fig. 1 (b) and Fig. 2(b) show the results using second-order elements (P2) for velocity and P1 for pressure. For comparison, Fig. 1(c) and Fig. 2(c) present the results using P1 for both velocity and pressure without GLS stabilization. This formulation does not satisfy the Ladyzhenskaya–Babuška–Brezzi (LBB) condition. It is evident that without GLS stabilization, the pressure field present spurious and oscillatory results. Whereas the application of GLS stabilization significantly improves the stability and accuracy of the numerical solution.

A similar GLS stabilization form is applied to the CHT equation. With $\mathscr{T}$ as the appropriate trial function space for the temperature and $\widetilde{\mathscr{T}}$ as the corresponding test function space, the weak form of the CHT equation is derived as : find $\overline{T}\in\mathscr{T}$ such that $\forall\overline{T}_w\in\widetilde{\mathscr{T}}$

$$\begin{aligned}\mathscr{W}_{T}(\overline{T})=&\int_{\Omega}\left[\widetilde{\overline{\gamma}}^{2p}RePr(\overline{\mathbf{u}}\cdot\overline{\nabla T})-\overline{Q}(\widetilde{\overline{\gamma}})\right]\overline{T}_w+\overline{k}(\widetilde{\overline{\gamma}})\overline{\nabla T}\cdot\overline{\nabla T}_w d\Omega\\&+\int_{\Gamma_N}g_{TN}\overline{T}_w d\Gamma+\sum_{e=1}^{n_{el}}\int_{\Omega^{e}}\tau_{PSPGT}\widetilde{\overline{\gamma}}^{2p}RePr(\overline{\mathbf{u}}\cdot\overline{\nabla T}_w)\mathscr{R}(\overline{T})d\Omega=0,\\&\forall\overline{T}_w\in\widetilde{\mathscr{T}}\end{aligned}\tag{14}$$

where $\mathscr{R}(\overline{T})=\widetilde{\overline{\gamma}}^{2p}RePr(\overline{\mathbf{u}}\cdot\overline{\nabla T})+\overline{\nabla}\cdot(-\overline{k}(\widetilde{\overline{\gamma}})\overline{\nabla T})-\overline{Q}(\widetilde{\overline{\gamma}})$ is the residual and τ_{PSPGT} is the stabilization parameter, which is chosen as $\tau_{PSPGT}=1/\sqrt{\left(2\widetilde{\overline{\gamma}}^{2p}RePr\|\overline{\mathbf{u}}\|/h_e\right)^2+\left(4\overline{k}(\widetilde{\overline{\gamma}})/h_e^2\right)^2}$ [63].

The effectiveness of the GLS stabilization term for the CHT equation is illustrated in Fig. 3. In Fig. 3(a), P1 is used for temperature with GLS stabilization. Fig. 3(b) show the results using P1 for temperature without GLS stabilization. It is evident that without GLS stabilization, the temperature field present spurious and oscillatory results, indicating instability in the numerical solution. Therefore, the application of GLS stabilization significantly improves the stability and accuracy of the numerical solution.

With $\mathscr{g}$ representing the appropriate trial function space for the filtered design variable $\widetilde{\gamma}$ and $\widetilde{\mathscr{g}}$ as the corresponding test function space, the weak form of the filter equation is derived as: find $\widetilde{\gamma}\in\mathscr{g}$ such that

$$\begin{aligned}\mathscr{W}_{\tilde{\gamma}}\left(\widetilde{\gamma}_w\right)=&\int_{\Omega}r^2\nabla\widetilde{\gamma}\cdot\nabla\widetilde{\gamma}_w+(\widetilde{\gamma}-\gamma)\widetilde{\gamma}_w d\Omega=0,\\&\forall\widetilde{\gamma}_w\in\widetilde{\mathscr{g}}.\end{aligned}\tag{15}$$

Based on the aforementioned weak forms of the PDEs, the continuous adjoint analysis of the TO problem can be implemented.

2.4. Continuous adjoint analysis

The solution of the TO problem in Eq. (15) can be achieved by using an iterative procedure based on the gradient information of the objective and constraints. Considering the large number of design variables inherent in the TO problem, an efficient method using the Lagrangian multiplier approach and the continuous adjoint method is necessary to obtain the gradient [64]. The continuous adjoint method enables us to obtain the gradient by solving the adjoint PDEs. The formulation of the augmented Lagrangian is expressed as

$$\mathscr{L}=J_{th}+\mathscr{W}_{up}(\overline{\mathbf{u}}_a,\overline{p}_a)+\mathscr{W}_{T}(\overline{T}_a)+\mathscr{W}_{\tilde{\gamma}}\left(\widetilde{\gamma}_a\right)\tag{16}$$

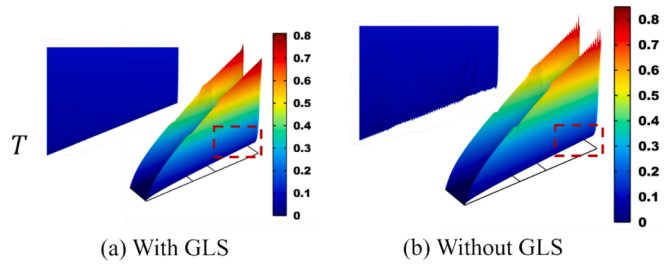

Fig. 3. Numerical solutions of temperature for the CHT equation. (a) P1 for temperature with GLS stabilization. (b) P1 for temperature.

where $(\overline{\mathbf{u}}_a, \overline{p}_a) \in \mathscr{V} \times \mathscr{Q}$, $\overline{T}_a \in \widetilde{\mathscr{T}}$, and $\widetilde{\gamma}_a \in \widetilde{\mathscr{G}}$ denote the adjoint variables. The total variational of $\mathscr{L}$ is

$$\delta\mathscr{L} = \delta_{\overline{\mathbf{u}}}\mathscr{L} + \delta_{\overline{p}}\mathscr{L} + \delta_{\overline{T}}\mathscr{L} + \delta_{\widetilde{\gamma}}\mathscr{L} + \delta_{\gamma}\mathscr{L}. \tag{17}$$

Then, the adjoint equations can be obtained as

$$\begin{cases} \delta_{\overline{T}}\mathscr{L} = 0 \\ \delta_{\overline{\mathbf{u}}}\mathscr{L} + \delta_{\overline{p}}\mathscr{L} = 0 \\ \delta_{\widetilde{\gamma}}\mathscr{L} = 0 \end{cases}. \tag{18}$$

Solving the adjoint equations enables the computation of the adjoint sensitivity used to update the design variables.

The total variational of the augmented Lagrangian $\mathscr{L}$ with respect to $\delta\gamma$ can be taken to derive the adjoint sensitivity as

$$\delta_{\gamma}\mathscr{L} = \int_{\Omega} -\widetilde{\gamma}_a \delta\gamma d\Omega. \tag{19}$$

Based on the adjoint sensitivity, the design variables can be iteratively evolved to optimize the microchannel heat sink.

3. Numerical implementation

The TO problem in Eq. (12) is solved using an iterative approach, where the design variables are evolved toward optimality based on the gradient information (Table 1). The gradient information is determined via the adjoint analysis of the TO problem [65]. After adjoint analysis,

Table 1
Procedure of the iterative approach for solving the TO problem.

1.	Give the initial value of the design variable γ;
2.	Solve the Navier–Stokes equations and convective heat transfer equation using the finite-element method;
3.	Solve the adjoint equations and compute the adjoint derivative and the corresponding objective value;
4.	Smooth the adjoint derivative;
5.	Update the design variable using the method of moving asymptotes;
6.	Check for convergence; if the stopping conditions are not satisfied, go to 2;
7.	Postprocessing

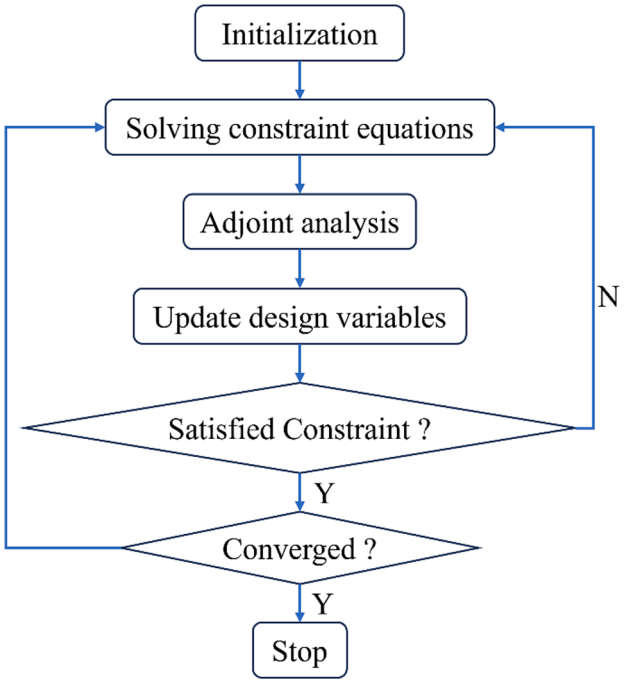

Chart 1. Flowchart of the TO.

an iterative procedure that covers the following steps can be performed to solve the TO problem.

For convergence, either the change in the objective function values in five consecutive iterations satisfies $\sum_{i=0}^{4}|J_{thk-i} - J_{thk-i-1}|/5J_{thk} < 10^{-3}$ in the k-th iteration step or the maximal iteration number 230, has been reached, where J_{thk} denotes the value of the objective function in the k-th iteration. The maximum iteration number of 230 was chosen based on numerical tests, the convergence process of TO for the first numerical example in both 3D and 2D is shown in Fig. 4.

In this iterative procedure, the finite-element solutions of all partial differential equations and corresponding adjoint equations are implemented using the finite-element software COMSOL Multiphysics (http://www.comsol.com). Discretization is performed using linear elements for all spatially distributed variables. The complete algorithmic process of the TO is illustrated in Chart 1.

4. Numerical investigation of microchannel heat sink

TO for microchannel heat sinks is investigated using both 2D and 3D models. The mesh nodes are adopted as design variables. The study focused on the evaluation of the impact of four critical parameters on the improvement of heat transfer while maintaining the constraints of the power dissipation. Specifically, the effects of *Re*, the *Pe*, the synergy between these two factors, and the ratio of solid-to-fluid thermal con-

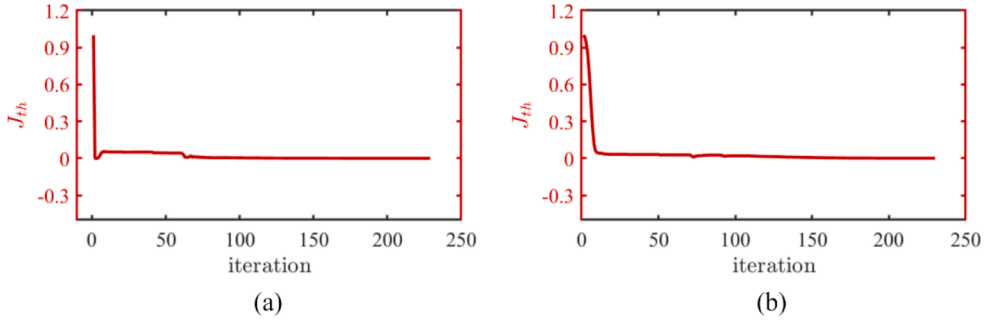

Fig. 4. The convergence process of TO for the first numerical example in both 2D and 3D, (a) 2D, (b) 3D.

ductivity (k_r) are systematically examined. To ensure a fair and consistent comparison, a control variable approach is adopted, maintaining identical algorithm parameters, boundary conditions, finite-element mesh, and constraints across all numerical examples. Fig. 5 presents a schematic diagram of a microchannel heat sink.

4.1. 2D numerical examples

This section presents numerical examples illustrating 2D TO of microchannel heat sinks. The determination of parameter selection in this section is based on previous research [45,66] as well as practical application and numerical test.

As the height of the microchannel heat sink is several hundred microns, heat is mainly dissipated from the microchannel in the horizontal plane through the coolant. Consequently, it is assumed that there is minimal temperature difference in the vertical direction, leading to neglect of heat transfer in this direction and yielding a simplified 2D model as described below.

4.1.1. Design domain

The 2D numerical examples use an identical design domain and boundary conditions to ensure equitable comparisons. Fig. 6 illustrates the design domain for the 2D simplified model for the TO problem of the microchannel heat sink. The inlet flow features a prescribed parabolic dimensionless velocity profile $\overline{\mathbf{u}}_{in}$, with a maximum dimensionless velocity $\|\overline{\mathbf{u}}_{in}\| = 100$ and a constant dimensionless temperature $\overline{T}_{in} = 0$. The outlet flow is characterized by the natural boundary conditions for dimensionless temperature and pressure $\overline{p} = 0$. All the other boundaries Γ_w are treated as no-slip and adiabatic. The fluid is assumed to be incompressible, Newtonian, and under the condition of the steady-state laminar flow. The inlet and outlet lengths are both set to 2L to achieve the fully developed flow.

This study uses a uniform design variable with $\gamma = 0.5$ as the initial guess. The volume occupied by fluid material within the design domain is constrained to 50 % of the total volume. For comparison, the constraint value for dimensionless power dissipation is set to 4.46×10^7 based on numerical tests. The other parameters used in the TO remain consistent across all the numerical examples.

The discretization of the 2D design domain is illustrated in Fig. 7. A structured finite element mesh is employed to divide the domain into discrete elements, ensuring uniform representation of the design space for TO.

4.1.2. Effect of the Reynolds number

The effect of the Reynolds number on the 2D TO problem is discussed in this section. Fig. 8 presents the results varying along with the *Re* ranging from 10 to 120 while maintaining the constant *Pe* of 100. The parameters for TO in this section are provided in Table 2.

In Fig. 8, the increase in the *Re* can result in more bifurcated microchannels, and also more number of solid islands within the design domain. This phenomenon could be attributed to the fact that under identical inlet velocity and fluid dissipation power, an increase in the *Re* will result in a reduction of the first term in the formula for the fluid

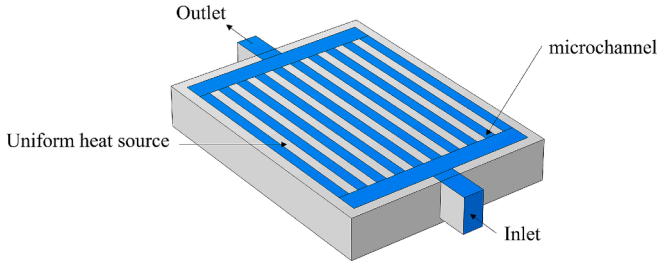

Fig. 5. Schematic of a microchannel heat sink.

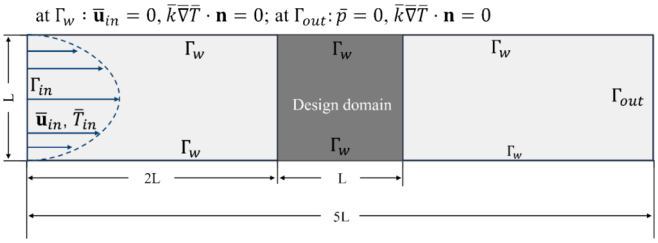

Fig. 6. Design domain of the 2D TO problem.

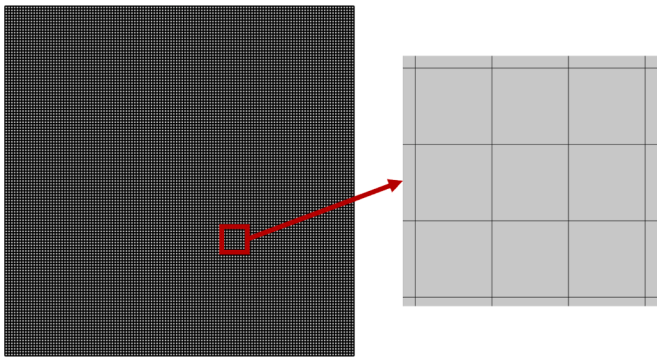

Fig. 7. The discretized density variable field in 2D design domain.

dissipation power (Eq.(11)). To maintain consistent fluid dissipation power, the structure produced by the TO will induce an augmentation of velocity variation. With increased bifurcations and islands within the microchannels, there is a greater velocity variation compared with flat microchannels. This description is supported by the relative value of the viscous dissipation of the fluid J_{Fn} curve and the relative value of the dimensionless pressure drop Δp curve depicted in Fig. 9. By adjusting the *Re*, the objective function exhibits a maximum decrease of 79.37 %. Therefore, as the *Re* increases, microchannels evolve to become more complex while adhering to the constraint of total dissipation power. Notably, the microchannel gradually tapers in width. The Δp curve also demonstrates that the impact of the viscous dissipation of fluid constraint is analogous to that of the pressure drop constraint. As the number of bifurcated microchannels and solid islands increases within the design domain, the contact interface between fluid and solid is augmented, thereby facilitating enhanced heat transfer into the fluid. This description is supported by the relative value of the objective J_n curve and the relative value of the maximum dimensionless temperature in the solid domain T_n curve depicted in Fig. 9. As the *Re* increases, the microchannel constricts, resulting in an escalation of local fluid velocity. Consequently, the maximum temperature differential within the solid domain reduces and the high temperature region shifts toward the outlet. This description is supported by the relative value of the maximum dimensionless temperature difference in the solid domain ΔT curve depicted in Fig. 9.

Owing to the consistent utilization of the same design domain, inlet velocity, viscous dissipation of fluid, fluid density, heat conductivity, and specific heat capacity in this section, an increase in *Re* suggests a reduction in fluid viscosity. When considering a coolant with equivalent thermal performance, lower viscosity proves to be more effective in reducing pressure drop.

4.1.3. Effect of the Péclet number

The effect of the *Pe* on the 2D TO problem is discussed in this section. Fig. 10 presents the results that vary with *Pe* ranging from 190 to 300 while maintaining the constant *Re* of 50. The parameters for TO in this section are provided in Table 3.

Analysis of the density variable shown in Fig. 10 reveal the variations

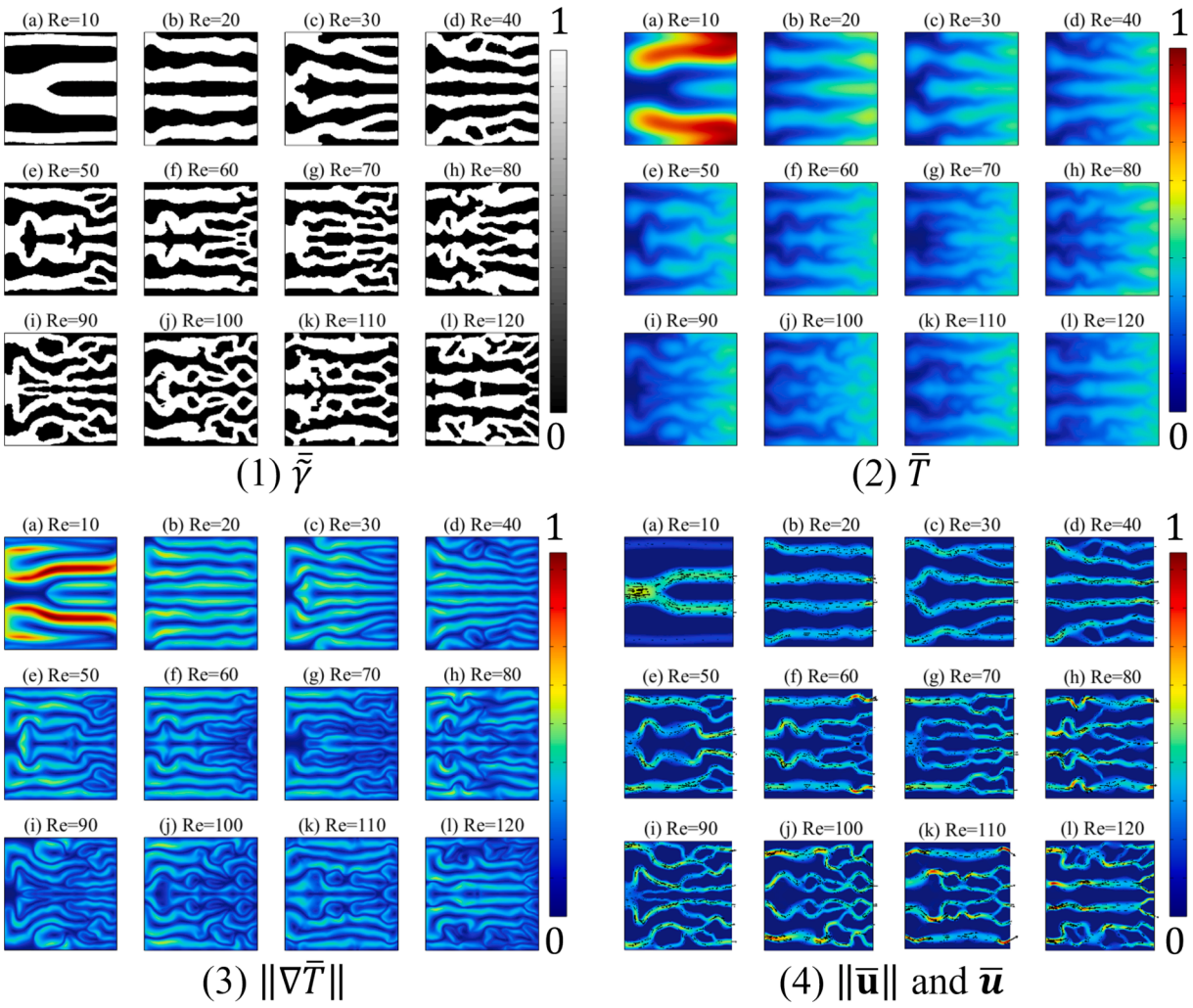

Fig. 8. TO results for different *Re*. (1) Distribution of the density variable, (2) distribution of the temperature, (3) distribution of the magnitude of the temperature gradient, (4) distribution of the fluidic velocity.

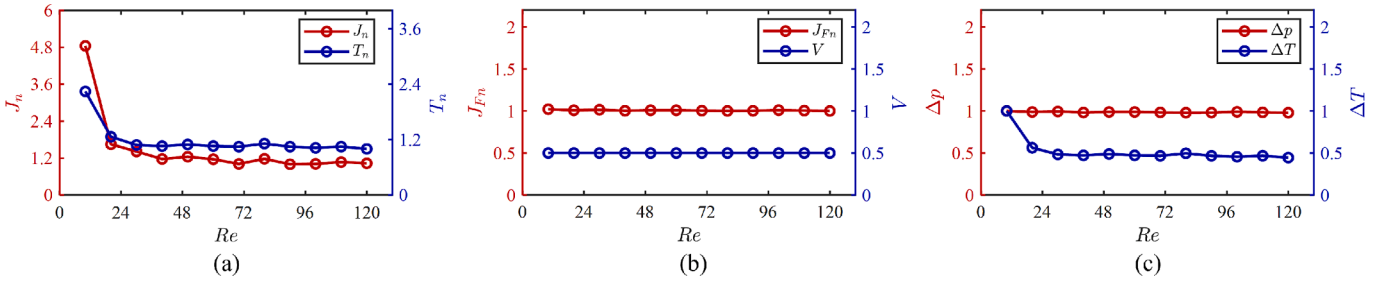

Fig. 9. Relative changes in the multiple indicators of the optimized structure with *Re*. (a) $J_n = J_{th}/\min\{J_{th}\}$ and $T_n = \overline{T}_{\max}/\min\{\overline{T}_{\max}\}$, (b) $J_{Fn} = J_F/J_{Fc}$ and the volume fraction of the fluid domain V, (c) $\Delta p = (\bar{p}_{in} - \bar{p}_{out})/\max\{(\bar{p}_{in} - \bar{p}_{out})\}$ and $\Delta T = \Delta\overline{T}/\max\{\Delta\overline{T}\}$.

Table 2
The parameter for the TO.

k_r	J_F	r	M_s	Pe
1	4.46×10^7	$1.2M_s$	$L/125$	100

of the optimized structure along with the change in the *Pe*. The distribution of the temperature is directly affected by the *Pe*, which in turn affects the objective function. Thus, the *Pe* can only indirectly impact the flow field by optimizing the objective function. Therefore, the effect of the *Pe* on the layout of the microchannels is complicated. Furthermore, the uniform velocity distribution remains largely unaltered. As the *Pe* increases, the temperature distribution within the solid domain becomes increasingly uniform. Such a description is supported by the ΔT curve shown in Fig. 11. This is because as the *Pe* increases, the convective heat transfer of the fluid correspondingly increases. Due to the consistent utilization of the same design domain, inlet velocity, viscous dissipation of fluid, fluid density, heat conductivity, and viscosity in this section, an increase in the *Pe* indicates an increase in the specific heat capacity of fluid. When considering a coolant for microchannel heat sinks, a higher specific heat capacity proves to be more uniform in temperature

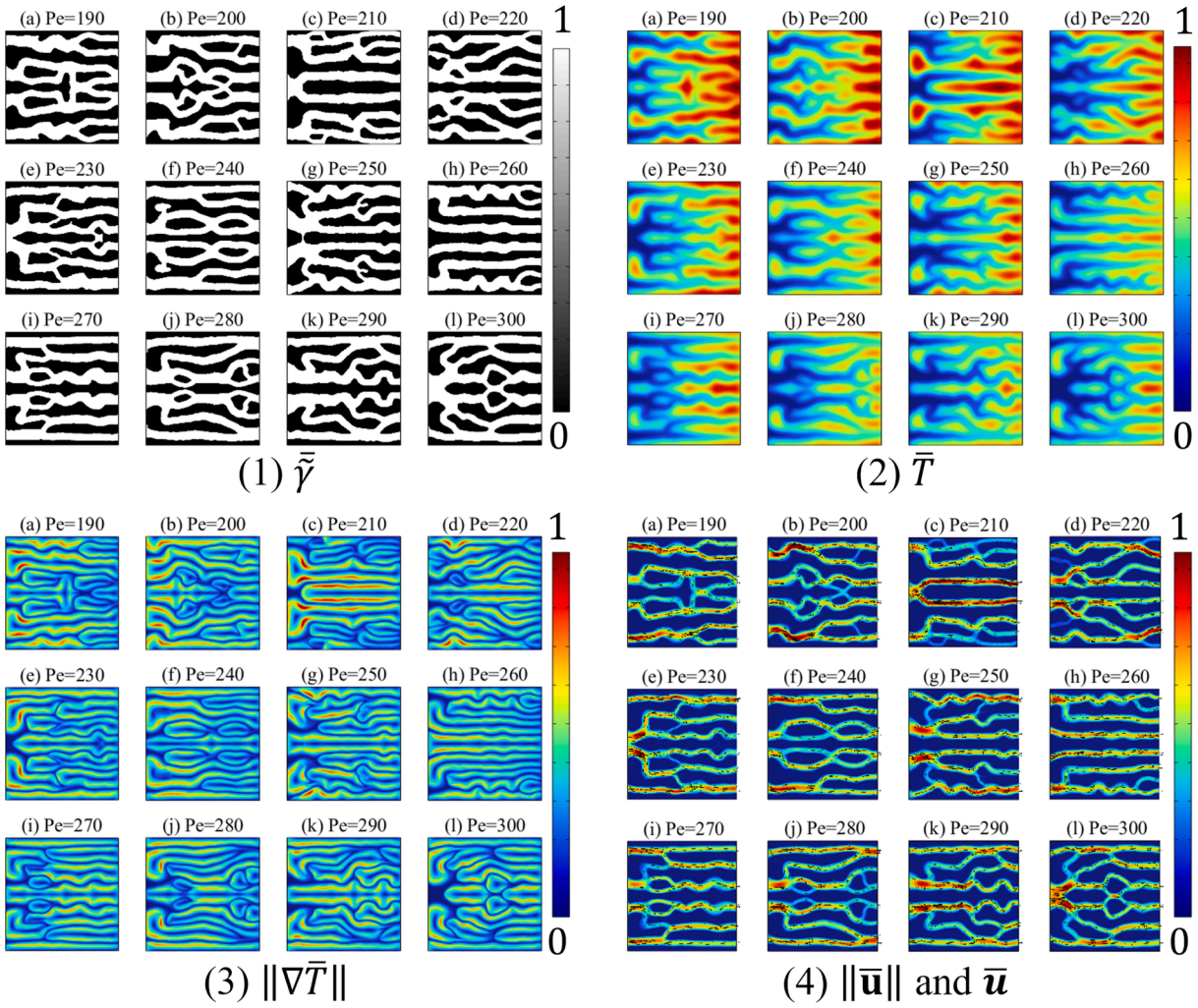

Fig. 10. TO results for different *Pe*. (1) Distribution of the density variable, (2) distribution of the temperature, (3) distribution of the magnitude of the temperature gradient, (4) distribution of the fluidic velocity.

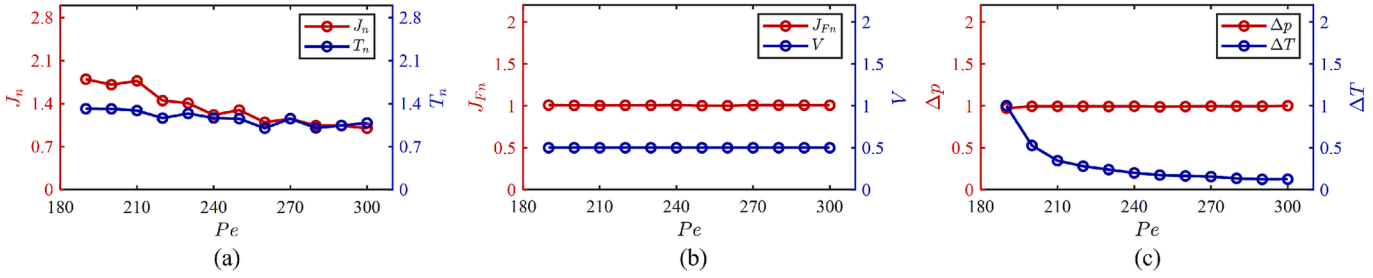

Fig. 11. Relative changes in the multiple indicators of the optimized structure with *Pe*. (a) $J_n = J_{th}/\min\{J_{th}\}$ and $T_n = \bar{T}_{\max}/\min\{\bar{T}_{\max}\}$, (b) $J_{Fn} = J_F/J_{Fc}$ and the volume fraction of the fluid domain V, (c) $\Delta p = (\bar{p}_{in} - \bar{p}_{out})/\max\{(\bar{p}_{in} - \bar{p}_{out})\}$ and $\Delta T = \Delta\bar{T}/\max\{\Delta\bar{T}\}$.

distribution.

Fig. 11 demonstrates that J_n and T_n fluctuating decrease and approach a limit as *Pe* increases. By adjusting *Pe*, the objective function exhibits a maximum decrease of 44.4%. The fact that J_{Fn} and Δp remain unchanged demonstrates that the impact of the viscous dissipation of fluid constraint is analogous to that of the pressure drop constraint.

Table 3
Parameter for the TO.

k_r	J_F	r	M_s	Re
1	4.46×10^7	$1.2M_s$	$L/125$	50

4.1.4. *Synergistic effect of the Reynolds and Péclet numbers*

The synergistic effect of the *Re* and *Pe* in the 2D TO problem is discussed in this section. Fig. 12 presents the results that vary with the *Re* ranging from 10 to 120 and the corresponding synergistic *Pe* ranging from 20 to 240. The parameters for TO in this section are provided in Table 4. In Fig. 12, the synergistic increase in the *Re* and *Pe* can result in more bifurcated microchannels, and also more number of solid islands within the design domain. The velocity distribution within the microchannel becomes increasingly uniform. The maximum thickness of the

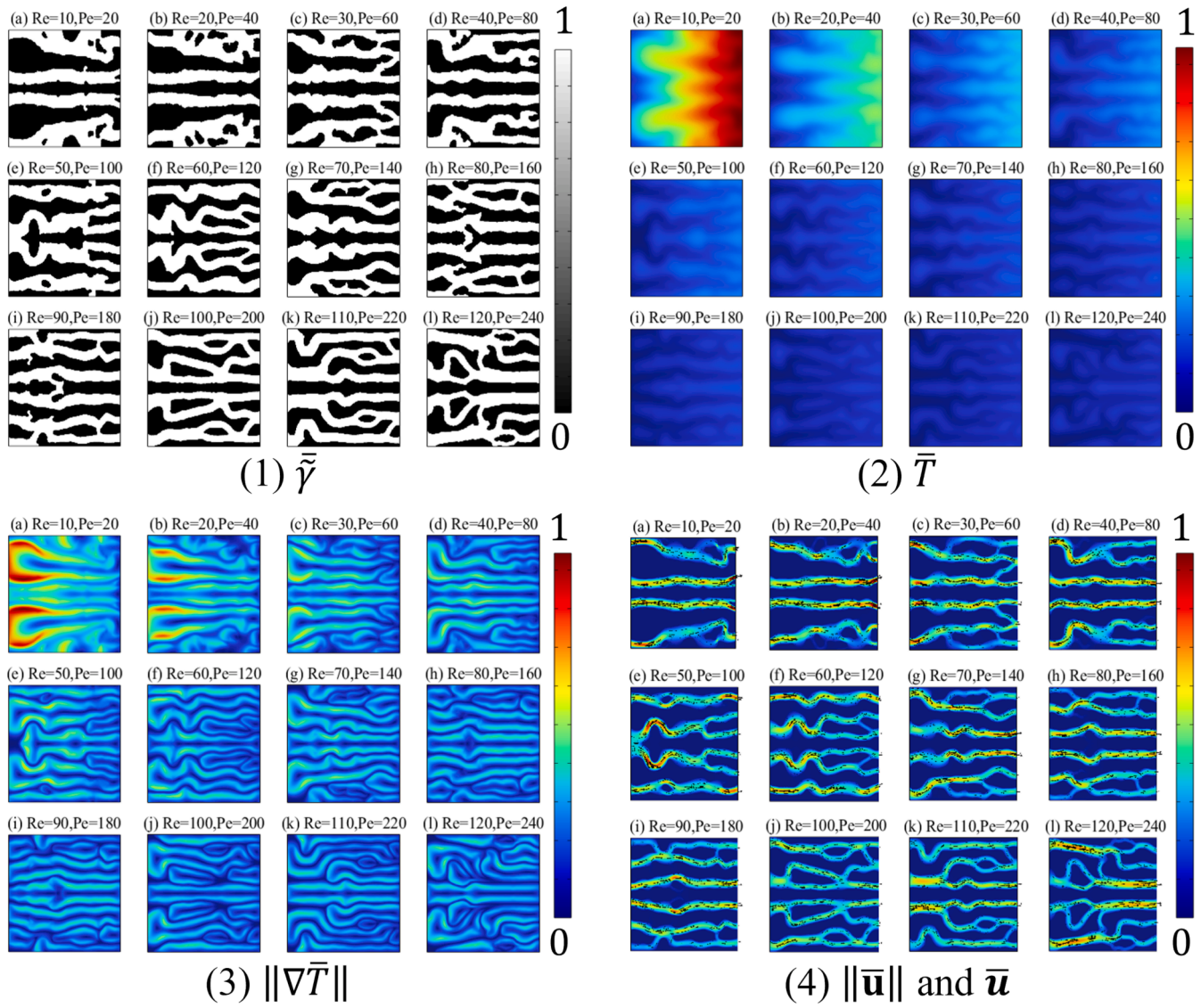

Fig. 12. TO results for the different synergies of *Re* and the *Pe*. (1) Distribution of the density variable, (2) distribution of the temperature, (3) distribution of the magnitude of the temperature gradient, (4) distribution of the fluidic velocity.

microchannel walls gradually decreases, thereby reducing heat accumulation in localized solid regions and lowering temperatures. The temperature distribution within the solid domain becomes increasingly uniform. This description is supported by the ΔT curve presented in Fig. 13. Due to the consistent utilization of the same design domain, inlet velocity, viscous dissipation of fluid, fluid-specific heat capacity, heat conductivity, and viscosity in this section, a synergistic increase in *Re* and *Pe* indicates an increase in fluid density. When considering a coolant for microchannel heat sinks, a higher fluid density proves to be more uniform in temperature distribution.

Fig. 13 demonstrates that J_n and T_n, with a synergistic increase in *Re* and *Pe*, decrease and approach a limit. By synergistically adjusting *Re*

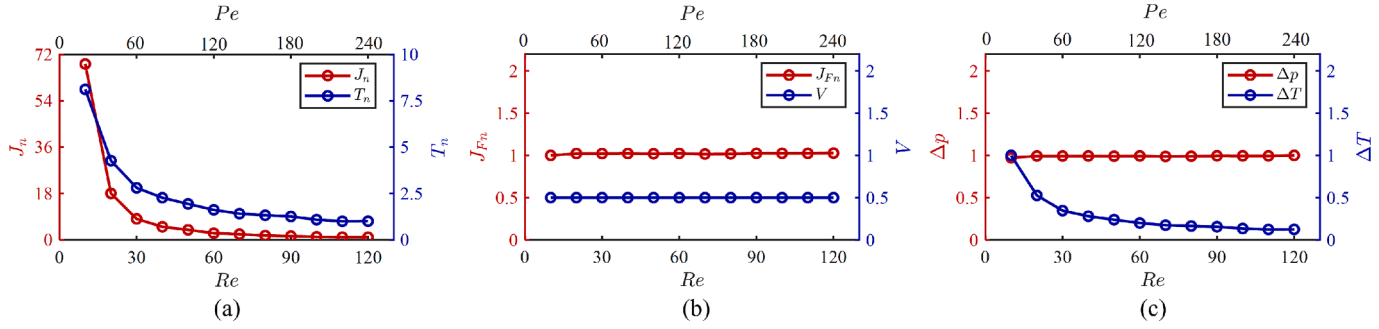

Fig. 13. Relative changes in the multiple indicators of the optimized structure with *Re* and *Pe*. (a) $J_n = J_{th}/\min\{J_{th}\}$ and $T_n = \overline{T}_{\max}/\min\{\overline{T}_{\max}\}$, (b) $J_{Fn} = J_F/J_{Fc}$ and the volume fraction of the fluid domain V, (c) $\Delta p = (\bar{p}_{in} - \bar{p}_{out})/\max\{(\bar{p}_{in} - \bar{p}_{out})\}$ and $\Delta T = \Delta\overline{T}/\max\{\Delta\overline{T}\}$.

and *Pe*, the objective function exhibits a maximum decrease of 98.54%. The fact that J_{Fn} and Δp remain unchanged demonstrates that the impact of the viscous dissipation of fluid constraint is analogous to that of the pressure drop constraint.

4.1.5. Effect of the ratio of solid-to-fluid thermal conductivity

The effect of the k_r on the 2D TO problem is discussed in this section. Fig. 14 presents the results that vary with k_r ranging from 0.01 to 600. The *Pe* is constant at 100, and the *Re* is constant at 20. The parameters for TO in this section are provided in Table 5. In Fig. 14, the increase in k_r can decrease the contact interface area between the coolant and solid in microchannels. In other words, the increase in solid thermal conductivity leads to a reduction in the number of microchannels.

On the one hand, the higher thermal conductivity of solid facilitates the rapid transfer of heat to the solid–liquid interface, resulting in reducing the need for numerous microchannels within the solid domain. Because the heat from the solid transfers to the coolant through heat conduction at the solid–liquid interface. The boundary between the solid and fluid will lead to heat accumulation in the smaller connected solid domain, thereby increasing the probability of temperature increase. In this case, the effective way to enhance the transfer of heat from the solid domain to the coolant is to reduce the thickness of the boundary layer. In addition, the low velocity of the coolant will cause low heat convection transfer and result in heat accumulation at the solid domain. Therefore, it is necessary to enhance convective heat transfer in the fluid domain to increase the rate of heat dissipation from the heat sink. Thus, the microchannel structure obtained from the TO is designed with a large solid domain to promote a uniform temperature distribution with unobstructed and curved microchannels to reduce the thickness of the boundary layer, thereby improving the convective heat transfer of the liquid.

On the other hand, the higher thermal conductivity of fluid facilitates the rapid transfer of heat from the solid–fluid interface in fluid and can increase the contact area between the solid and fluid. In this case, the rapid heat transfer process in the fluid can cause more heat to be carried out of the heat sink by the bulk flow. Thus, microchannels characterized by a reduced connected solid domain and an increased solid–fluid interface area may lead to a more uniform temperature distribution and enhanced heat dissipation efficiency. However, the blocking structure may appear in the microchannels. This is because the objective function only focuses on the solid domain and can result in the development of branching structures that maximize the area of the solid–fluid interface while adhering to the constraint of the total dissipation power. As shown in Fig. 15, J_n, T_n, and ΔT, with an increase in k_r, decrease and approach a limit. By adjusting k_r, the objective function exhibits a maximum decrease of 99.43%. J_{Fn} and Δp remain unchanged.

4.2. 3D numerical examples

This section presents numerical examples illustrating the 3D TO of microchannel heat sinks. A stabilized finite-element formulation is employed to solve NS flows. Therefore, the use of mixed elements with equal-order interpolations for both velocity and pressure is permissible. A considerable reduction of the number of degrees of freedom leads to an enhancement in computational efficiency. However, the computational cost in 3D surpasses that of 2D. Based on the findings presented in Section 4.1, the governing principles of parameters influencing optimization structures in both 2D and 3D are correlated is hypothesized. Consequently, the values for the 3D parameters can be inferred based on the range of selection parameters in 2D. As a result, this approach leads to a reasonable reduction in the number of numerical examples in 3D.

Table 4
Parameter for the TO.

k_r	J_F	r	M_s
1	4.46×10^7	$1.2M_s$	$L/125$

4.2.1. Design domain

The 3D numerical examples use identical design domains and boundary conditions to ensure equitable comparisons. Fig. 16 illustrates the design domain for the full 3D model for the TO problem of the microchannel heat sink. The inlet flow features a prescribed dimensionless velocity $\overline{\mathbf{u}}_{in}$, with a constant dimensionless velocity $\|\overline{\mathbf{u}}_{in}\| = 100$, and a constant dimensionless temperature $\overline{T}_{in} = 0$. The outlet flow is characterized by the natural boundary condition for a dimensionless temperature and pressure $\overline{p} = 0$. All the other boundaries are treated as no-slip and adiabatic. The fluid is assumed to be incompressible, Newtonian, and under the condition of the steady-state laminar flow. The inlet and outlet lengths are both set to L to achieve a fully developed flow.

The study uses a uniform design variable with $\gamma = 0.5$ as the initial guess. The volume occupied by the fluid material within the design domain is constrained to 50 % of the total volume. For comparison, the constraint value for the dimensionless power dissipation is set to 6.08×10^6 based on numerical tests. The other parameters used in the TO remain consistent across all the numerical examples.

The discretization of the 3D design domain is illustrated in Fig. 17. A structured finite element mesh is employed to divide the domain into discrete elements, ensuring uniform representation of the design space for TO.

4.2.2. Effect of the Reynolds number

The effect of the *Re* on the 3D TO problem is discussed in this section. Fig. 18 presents the results that vary with the *Re* ranging from 70 to 120 while maintaining the constant *Pe* of 100. The parameters for TO in this section are provided in Table 6.

In Fig. 18, the increase in the *Re* can result in more bifurcated microchannels. And as the *Re* increases, the maximum temperature differential within the solid domain decreases and the high temperature region moves closer the outlet. This observation is consistent with the findings in the 2D case. Nevertheless, when the *Re* surpasses 100, some of the microchannels in the optimized result are blocked.

In the blocked microchannel, fluid infiltration into solid regions is advantageous in meeting the total dissipation power constraint by increasing value of the second term in J_F and in enhancing heat transfer from solid-to-fluid.

Fig. 19 shows that similar to the 2D case, J_n, T_n, and ΔT, with an increase in the *Re*, decrease and approach a limit. By adjusting *Re*, the maximum reduction of the objective function is 63.64 %. Contrary to the 2D case, the *Re* corresponding to the stationary state of J_n increases. J_{Fn} is almost unchanged, whereas Δp slightly decreases. This indicates that when fluid infiltrates into the blocking microchannel, the impact of the viscous dissipation of fluid constraint is not analogous to that of the pressure drop constraint.

4.2.3. Effect of the Péclet number

The effect of the *Pe* on the 3D TO problem is discussed in this section. The range of the *Pe* variation is ranging from 150 to 650, while maintaining the constant *Re* of 100. The parameters for TO in this section are provided in Table 7.

Analysis of the density variable presented in Fig. 20 revealed the variations of the optimized structure along with the change in the *Pe*. As the *Pe* increases, the temperature distribution within the solid domain becomes increasingly uniform. This trend is similar to that observed in the 2D case. However, the *Pe* corresponding to the stationary state of J_n markedly increases in the 3D case. As shown in Fig. 21, J_n, T_n, and ΔT, with an increase in the *Pe*, decrease and approach a limit. By adjusting *Pe*, the objective function exhibits a maximum decrease of 89.67%. The fact that J_{Fn} and Δp remain unchanged demonstrates that the impact of

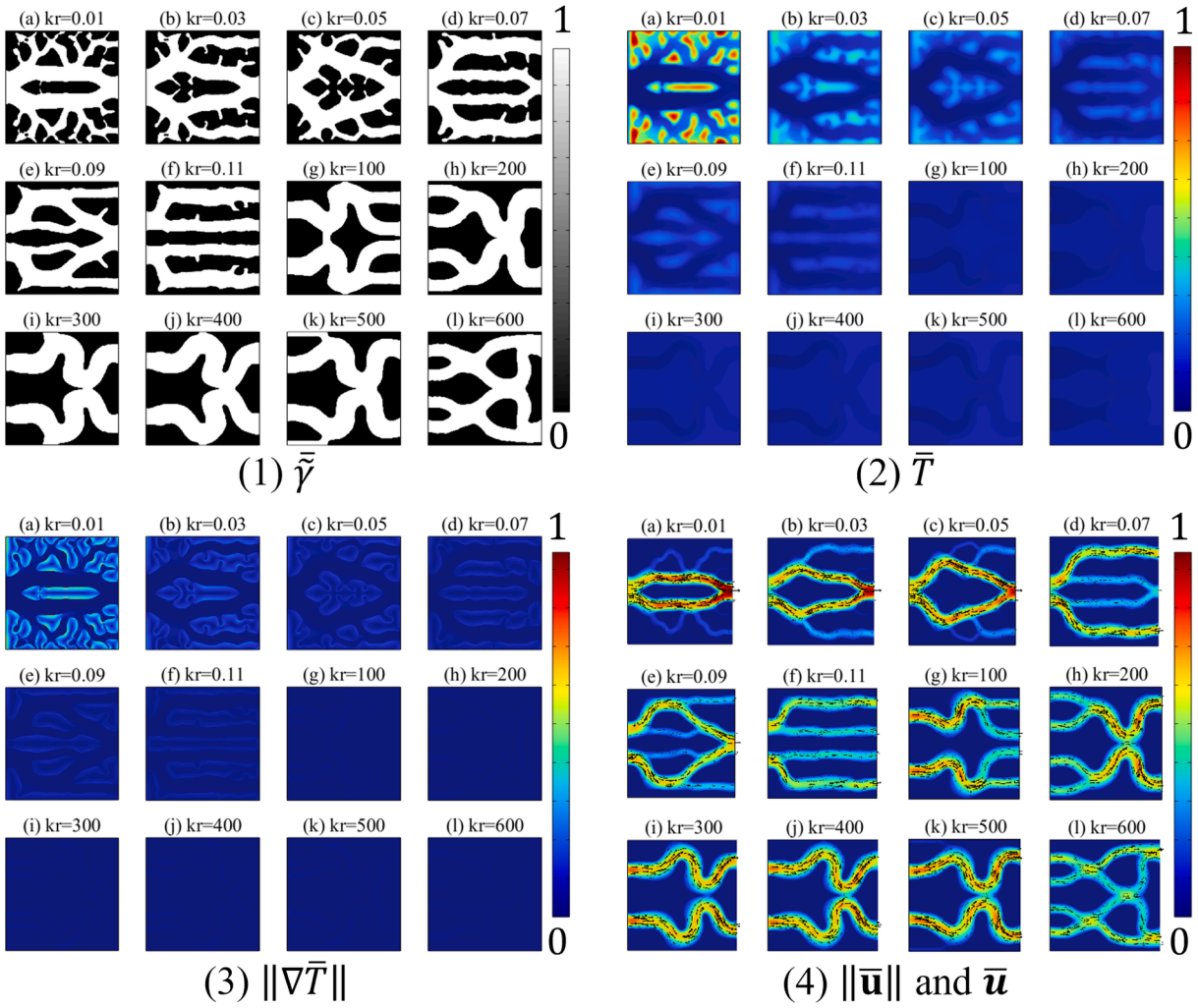

Fig. 14. TO results for the different k_r. (1) Distribution of the density variable, (2) distribution of the temperature, (3) distribution of the magnitude of the temperature gradient, (4) distribution of the fluidic velocity.

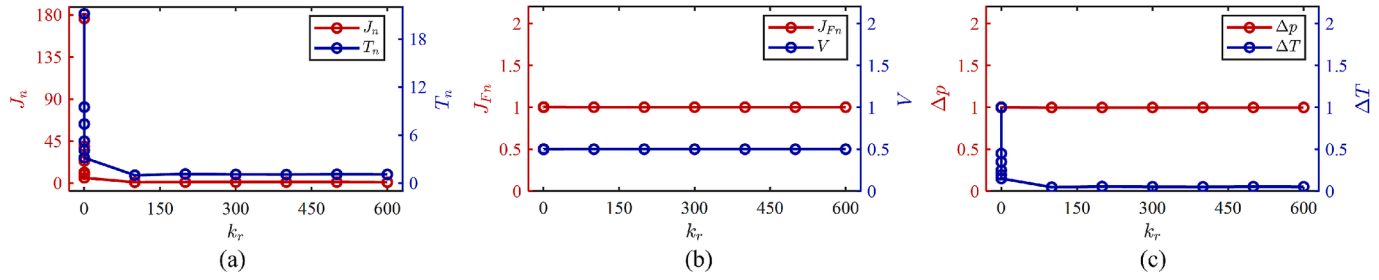

Fig. 15. Relative changes in the multiple indicators of the optimized structure with k_r. (a) $J_n = J_{th}/\min\{J_{th}\}$ and $T_n = \overline{T}_{\max}/\min\{\overline{T}_{\max}\}$, (b) $J_{Fn} = J_F/J_{Fc}$ and the volume fraction of the fluid domain V, (c) $\Delta p = (\overline{p}_{in} - \overline{p}_{out})/\max\{(\overline{p}_{in} - \overline{p}_{out})\}$ and $\Delta T = \Delta\overline{T}/\max\{\Delta\overline{T}\}$.

the viscous dissipation of fluid constraint is analogous to that of the pressure drop constraint.

4.2.4. Synergistic effect of the Reynolds and Péclet numbers

The synergistic effect of the *Re* and *Pe* on the 3D TO problem is discussed in this section. For comparison with the 2D case, the *Re* ranges from 70 to 120 and the corresponding synergistic *Pe* from 140 to 240. The parameters for TO in this section are provided in Table 8.

As shown in Fig. 22, a synergistic elevation in the *Re* and *Pe* has a negligible effect on the number of bifurcations of the microchannels and solid islands in the microchannels. The temperature distribution within the solid domain becomes increasingly uniform. Analysis of the corresponding 2D numerical example and Fig. 23 revealed that the selected *Re* and *Pe* fall within a range where they exert limited influence on the TO results. This indicates that the insights gained from the effects of

Table 5
Parameter for the TO.

J_F	r	M_s	Re	Pe
4.46×10^7	$1.2M_s$	$L/125$	20	100

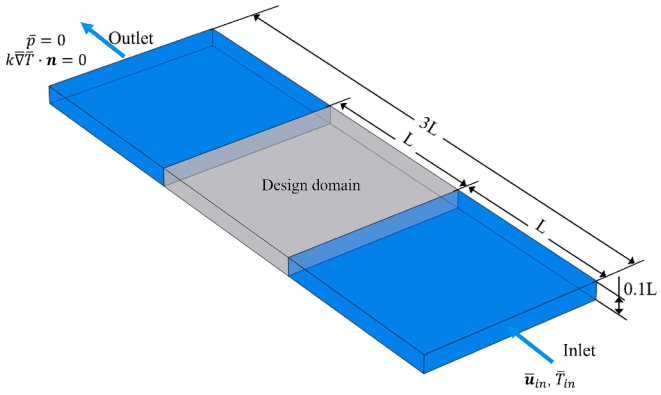

Fig. 16. Design domain for the 3D TO problem.

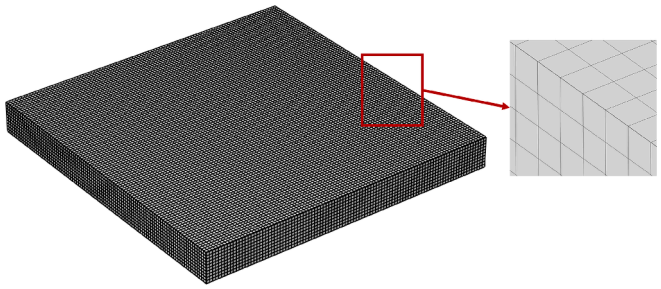

Fig. 17. The discretized density variable field in 3D design domain.

parameters on the 2D TO can guide the parameter selection for the 3D TO problems.

As shown in Fig. 23, J_n, T_n, and ΔT, with a synergistic variation of *Re* and *Pe*, are relatively stable. By synergistically adjusting *Re* and *Pe*, the objective function exhibits a maximum decrease of 12.08%. The fact that J_{Fn} and Δp remain unchanged demonstrates that the impact of the viscous dissipation of fluid constraint is analogous to that of the pressure drop constraint.

4.2.5. *Effect of the ratio of solid-to-fluid thermal conductivity*

The effect of the k_r on the 3D TO problem is discussed in this section. Fi.24 presents the results that vary with k_r ranging from 0.01 to 100. The *Pe* is constant at 200, and the *Re* is constant at 100. The parameters for TO in this section are provided in Table 9.

As shown in Fig. 24, the increase in k_r can decrease the contact interface area between the coolant and solid in microchannels. This trend is similar to that in the 2D numerical examples. Furthermore, the surface of the microfluidic channel adopts a "ripple"-like geometry, similar to the secondary design shown in [67]. This geometric configuration disrupts the boundary layer, consequently enhancing the convective heat transfer capacity. As shown in Fig. 25, J_n, T_n, and ΔT, with an increase in k_r, decrease and approach a limit. By synergistically adjusting *Re* and *Pe*, the objective function exhibits a maximum decrease of 98.02%. These findings are consistent with those in the 2D case. The fact that J_{Fn} and Δp remain unchanged demonstrates that the impact of the viscous dissipation of fluid constraint is analogous to that of the pressure drop constraint.

5. Discussion

Based on the findings of Tuckerman and Pease [7], a substantial pressure drop is necessary to induce turbulence within the microchannel. To achieve the objective of maximizing heat dissipation while minimizing pressure drop, this study focuses on the assumption of steady laminar flow of incompressible Newtonian fluid to develop a single-objective topology optimization model. The influence of material properties and flow conditions on the results of the topology optimization is explored by adjusting four parameters: Reynolds number, Péclet number, synergies of the Reynolds and Péclet numbers, and ratio of solid-to-fluid thermal conductivity. Due to the general nature of this study and the specific temperature-dependent characteristics of the coolant, the physical properties were not considered. In future research, we will explore the correlation between temperature and physical

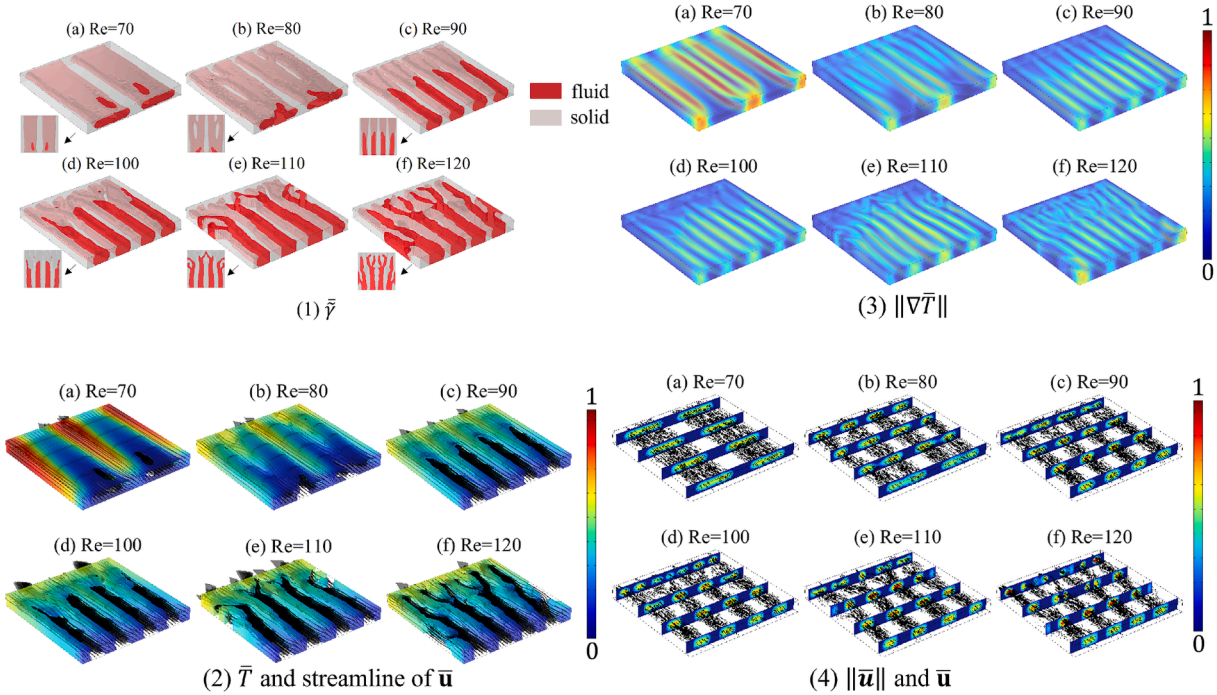

Fig. 18. TO results for the different *Re*. (1) Distribution of the density variable, (2) distribution of the temperature and streamline of $\bar{\mathbf{u}}$, (3) distribution of the magnitude of the temperature gradient, (4) distribution of the fluidic velocity.

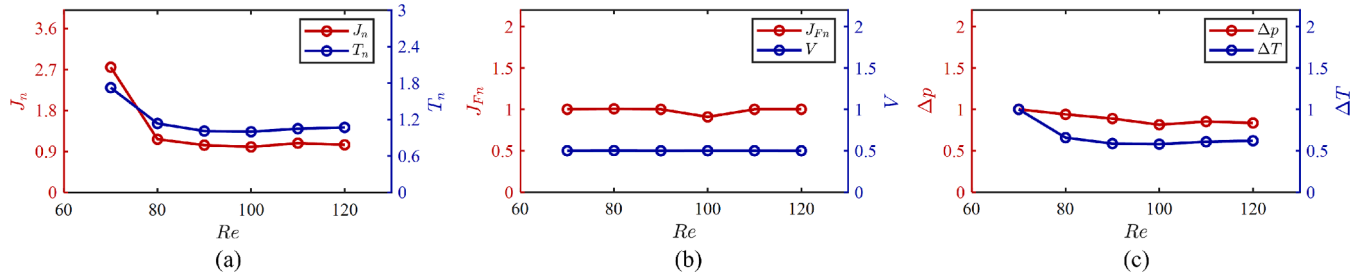

Fig. 19. Relative changes in the multiple indicators of the optimized structure with *Re*. (a) $J_n = J_{th}/\min\{J_{th}\}$ and $T_n = \overline{T}_{\max}/\min\{\overline{T}_{\max}\}$, (b) $J_{Fn} = J_F/J_{Fc}$ and the volume fraction of the fluid domain V, (c) $\Delta p = (\overline{p}_{in} - \overline{p}_{out})/\max\{(\overline{p}_{in} - \overline{p}_{out})\}$ and $\Delta T = \Delta\overline{T}/\max\{\Delta\overline{T}\}$.

Table 6
Parameter for the TO.

k_r	J_F	r	M_s	Pe
1	6.08×10^6	$2.4M_s$	$L/200$	100

Table 7
Parameter for the TO.

k_r	J_F	r	M_s	Re
1	6.08×10^6	$2.4M_s$	$L/200$	100

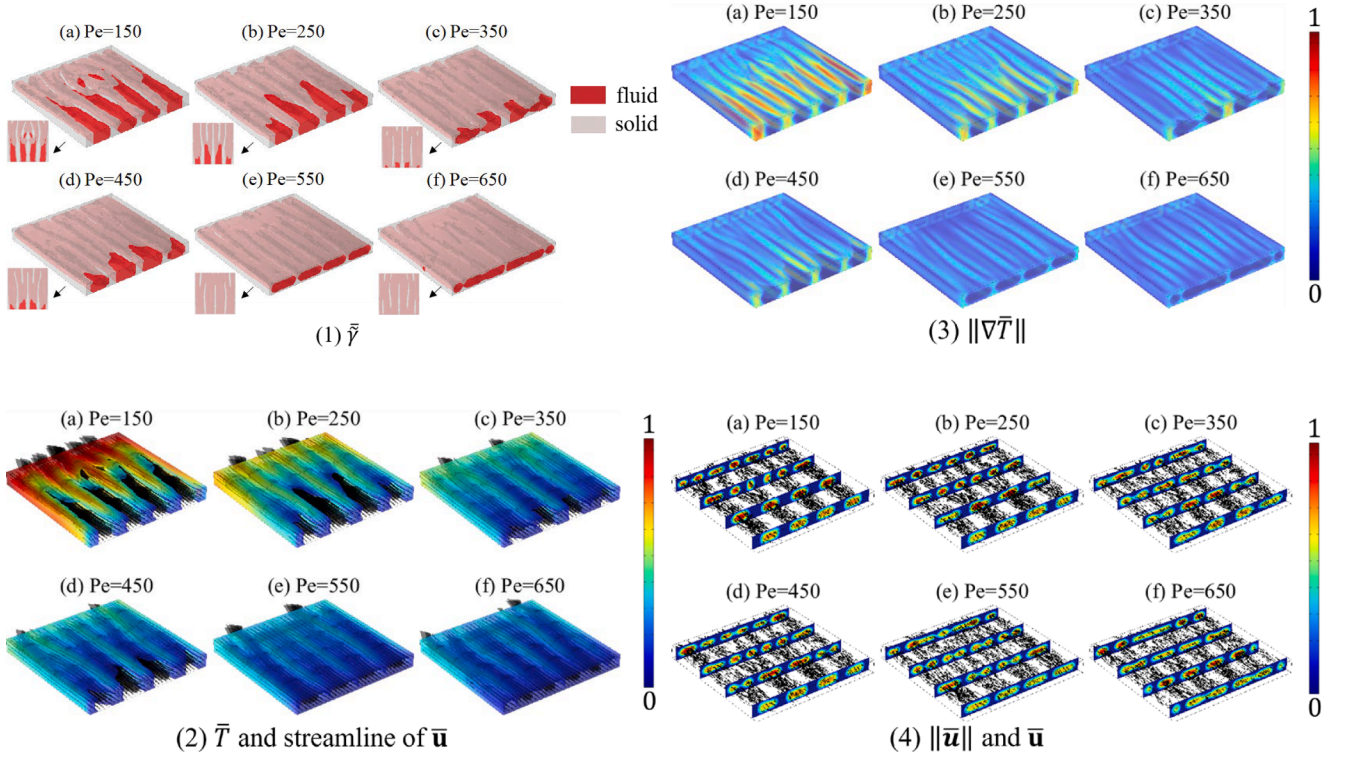

Fig. 20. TO results for the different *Pe*. (1) Distribution of the density variable, (2) distribution of the temperature and streamline of $\overline{\mathbf{u}}$, (3) distribution of the magnitude of the temperature gradient, (4) distribution of the fluidic velocity.

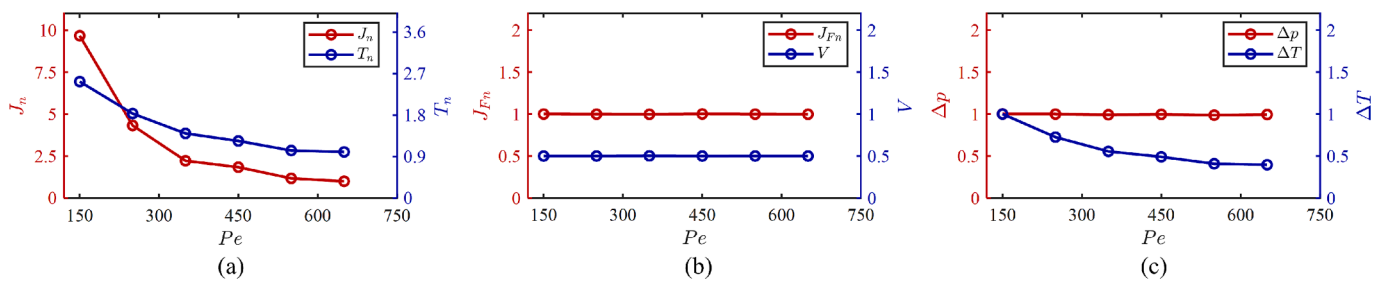

Fig. 21. Relative changes in the multiple indicators of the optimized structure with *Pe*. (a) $J_n = J_{th}/\min\{J_{th}\}$ and $T_n = \overline{T}_{\max}/\min\{\overline{T}_{\max}\}$, (b) $J_{Fn} = J_F/J_{Fc}$ and the volume fraction of the fluid domain V, (c) $\Delta p = (\overline{p}_{in} - \overline{p}_{out})/\max\{(\overline{p}_{in} - \overline{p}_{out})\}$ and $\Delta T = \Delta\overline{T}/\max\{\Delta\overline{T}\}$.

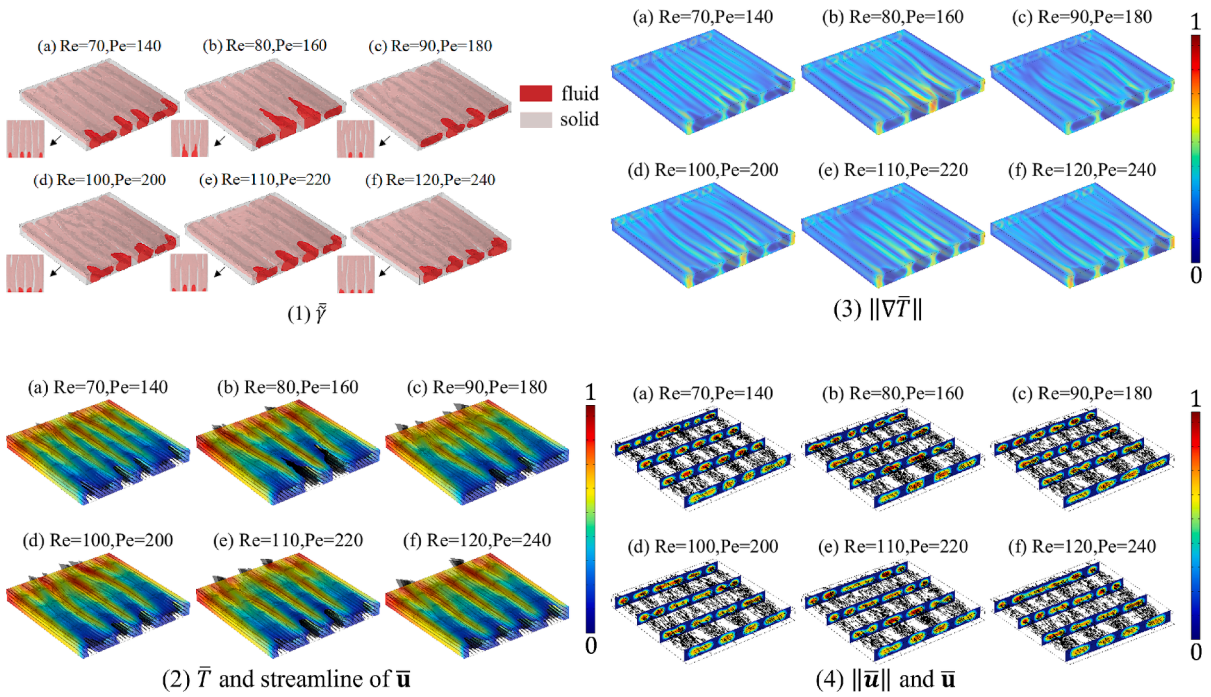

Fig. 22. TO results for the different synergies of the *Re* and the *Pe*. (1) Distribution of the density variable, (2) distribution of the temperature and streamline of $\overline{\mathbf{u}}$, (3) distribution of the magnitude of the temperature gradient, (4) distribution of the fluidic velocity.

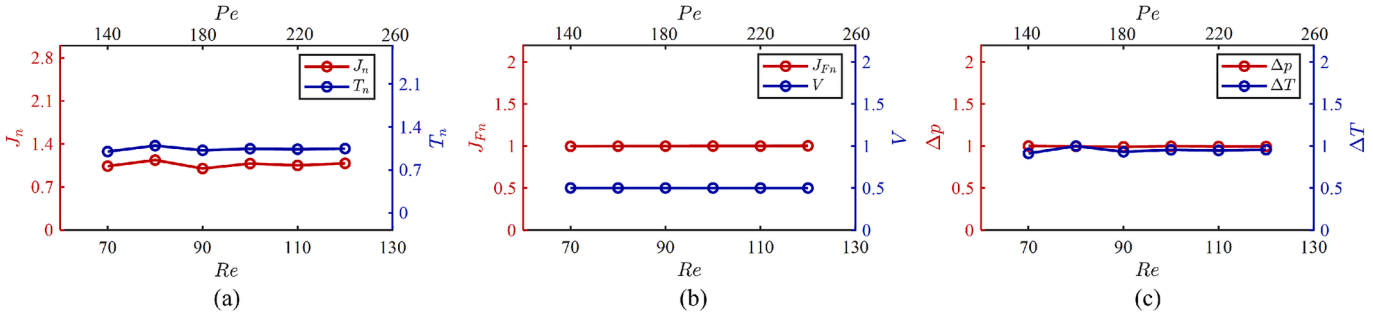

Fig. 23. Relative changes in the multiple indicators of the optimized structure with *Re* and *Pe*. (a) $J_n = J_{th}/\min\{J_{th}\}$ and $T_n = \overline{T}_{\max}/\min\{\overline{T}_{\max}\}$, (b) $J_{Fn} = J_F/J_{Fc}$ and the volume fraction of the fluid domain V, (c) $\Delta p = (\overline{p}_{in} - \overline{p}_{out})/\max\{(\overline{p}_{in} - \overline{p}_{out})\}$ and $\Delta T = \Delta\overline{T}/\max\{\Delta\overline{T}\}$.

Table 8
Parameter for the TO.

k_r	J_F	r	M_s
1	6.08×10^6	$2.4M_s$	$L/200$

characteristics while optimizing the design of microchannel heat sinks for a particular coolant.

Through the numerical examples, it was determined that the thermal performance of the optimal structure is constrained by the material properties and flow conditions. In this study, the thermal performance is represented by temperature uniformity. Therefore, when employing the topology optimization method proposed in this study to achieve a microchannel design, optimal thermal performance should be achieved by selecting a coolant with low viscosity, high fluid density, high specific heat capacity, and thermal conductivity similar to those of the solid material under known inlet velocity and pressure drop conditions.

An increase in the Reynolds and Péclet numbers has been shown to considerably enhance the temperature uniformity within the solid domain. This suggests that reducing viscosity and increasing the product of specific heat and density of the coolant is a promising direction for further investigation. Enhancing k_r is advantageous in facilitating a uniform temperature distribution. However, when $k_r > 25$, the advantages become negligible. Thus, in practice, the ratio of the thermal conductivity of the coolant to that of the solid is recommended not to exceed 25. In addition, it is advantageous for the product of the specific heat and density of the coolant to be maximized to facilitate temperature uniformity. The numerical examples demonstrate that as the viscosity of the coolant decreases, the width of the microchannel needs to become narrower and more tortuous. However, due to limitations in the topology optimization radius of the filter and finite-element mesh size, the minimum width of the microchannel is restricted. In practical design, it is necessary to reduce the width of microchannels and increase their quantity to enhance the thermal performance of microchannel heat exchangers. However, the current data in this study is insufficient for quantitative sensitivity analysis. Therefore, we planned to increase the numbers of data in future research to more comprehensively investigate parameter sensitivity. In addition, a database has been provided for the neural network of topology optimization.

In this study, a stabilized finite-element formulation to solve the Navier–Stokes flows is employed. A considerable reduction of the number of degrees of freedom leads to an enhancement in

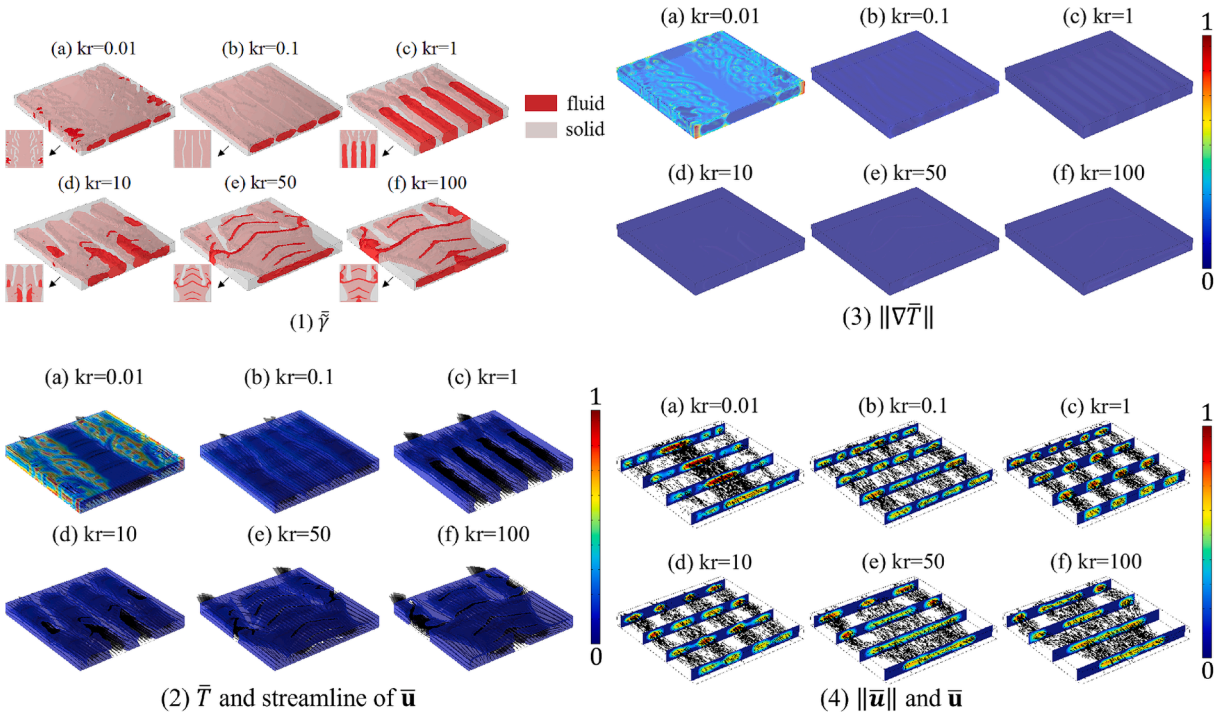

Fig. 24. TO results for the different k_r. (1) Distribution of the density variable, (2) distribution of the temperature and streamline of $\bar{\mathbf{u}}$, (3) distribution of the magnitude of the temperature gradient, (4) distribution of the fluidic velocity.

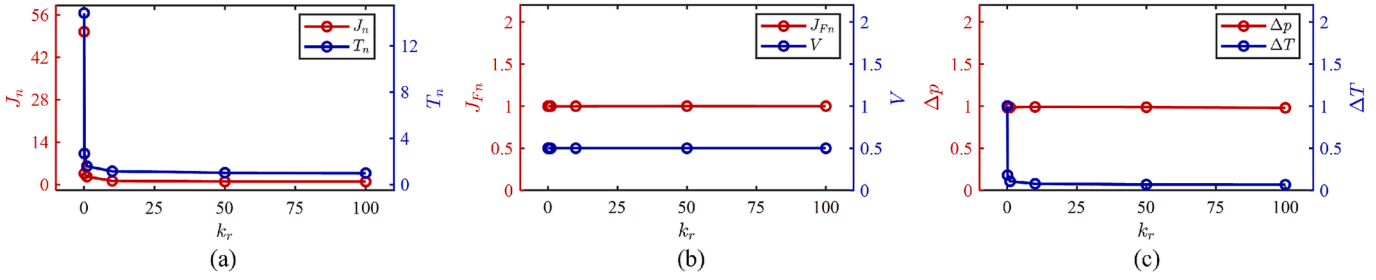

Fig. 25. Relative changes in the multiple indicators of the optimized structure with k_r. (a) $J_n = J_{th}/\min\{J_{th}\}$ and $T_n = \overline{T}_{\max}/\min\{\overline{T}_{\max}\}$, (b) $J_{Fn} = J_F/J_{Fc}$ and the volume fraction of the fluid domain V, (c) $\Delta p = (\bar{p}_{in} - \bar{p}_{out})/\max\{(\bar{p}_{in} - \bar{p}_{out})\}$ and $\Delta T = \Delta\overline{T}/\max\{\Delta\overline{T}\}$.

Table 9
Parameter for the TO.

J_F	r	M_s	Re	Pe
6.08×10^6	$2.4M_s$	$L/200$	100	200

computational efficiency with the use of mixed elements with equal-order interpolations for velocity and pressure. However, the computational cost in 3D surpasses that of 2D. The influence rule of the four parameters on the results of topology optimization is similar to those in the 2D and 3D cases. Hence, based on the numerical investigation, it is feasible to initially determine an appropriate combination of material properties and flow conditions through 2D topology optimization. Subsequently, an actual 3D optimized result can be achieved through 3D topology optimization. This approach has the potential to substantially reduce computational expenses and expedite the design iteration process.

The selection of algorithmic parameters for thermal–fluid coupling topology optimization is influenced by the physical parameters. Under the condition of identical total power dissipation, adjustment of physical parameters can lead to the generation of a structure that lacks physical significance, such as blockage of microfluidic channel with fluid penetration into the solid domain, where the fluid velocity approaches zero. This erroneous configuration can artificially inflate the heat dissipation of microchannel heat sinks.

Previous studies have demonstrated the effectiveness of topology optimization in heat sink topology. Therefore, this study systematically examined the parameters using the numerical method. Future work will involve experimental verification to further validate our findings.

6. Conclusions

This study investigated the influence of four parameters, namely, Reynolds number, Péclet number, synergies of the Reynolds and Péclet numbers, and ratio of solid-to-fluid thermal conductivity, on the performance of topologically optimized microchannel heat sinks. This study employed single-objective topology optimization methods while considering loose equality constraint on fluid energy dissipation and the volume fraction of fluid. Under the assumed conditions in this study, the main conclusions drawn are as follows.

The elevation of the four parameters has the potential to enhance temperature uniformity within the solid domain of the optimized structure in both the 2D and 3D cases. In the 2D case, the objective

function exhibited maximum decreases of 79.37%, 44.4%, 98.54%, and 99.43% for the four parameters, whereas in the 3D case, the maximum decreases were 63.64%, 89.67%, 12.08%, and 98.02%, respectively. This suggests that when employing topology optimization to design a microchannel heat sink, the utilization of a coolant with low viscosity, high specific heat, high thermal conductivity, and high density in combination with a solid material possessing high thermal conductivity has the potential to enhance the thermal and hydraulic performance of the optimized structure. Thus, microchannel heat sinks need to be tailored for the specific work conditions and characteristics of the intended object.

During the topology optimization design process, parameter selection relies on empirical knowledge and iterative experimentation, which can be a time-intensive endeavor, particularly when addressing the 3D problem. However, the influence rule of the four parameters on the results of the topology optimization is similar in the 2D and 3D cases. Thus, during the topology optimization of the 3D microchannel heat sink, these parameters can be identified through a 2D topology optimization in the parameter selection stage before implementing a 3D topology optimization to enhance the optimization design efficiency.

Topology optimization with least-squares for temperature in the solid domain as the objective and fluid energy dissipation as the relaxed equality constraint is valid in both 2D and 3D microchannel heat sinks. The least-squares objective for temperature in the solid domain can be used to measure the uniformity of temperature. The viscous dissipation of fluid constraint is analogous to that of the pressure drop constraint.

Funding

This research was supported by National Natural Science Foundation of China (Grant No. 51875545), Innovation Grant of Changchun Institute of Optics, Fine Mechanics and Physics (CIOMP), CAS Project for Young Scientists in Basic Research of China (Grant No. YSBR-066) and Science and Technology Development Program of Jilin Province of China (Grant No. SKL202302020), an EU2020 FET grant (TiSuMR, 737043), the DFG under grant KO 1883/20-1 Metacoils, funding within their famework of the German Excellence Intitiative under grant EXC 2082 “3D Matter Made to Order”, and from the VirtMat initiative “Virtual Materials Design”.

Declaration of competing interest

The authors declare that they have no known competing financial interests or personal relationships that could have appeared to influence the work reported in this paper.

Data availability

The authors do not have permission to share data.

References

[1] X. Wang, C. Liu, Y. Wei, S. Feng, D. Sun, H. Cheng, Three-dimensional transistors and integration based on low-dimensional materials for the post-Moore’s law era, Mater Today 63 (2023) 170–187, https://doi.org/10.1016/j.mattod.2022.11.023.
[2] S.S. Hsieh, S.Y. Luo, Droplet Impact Dynamics and Transient Heat Transfer of a Micro Spray System for Power Electronics Devices, Int. J. Heat Mass Tran. 92 (2016) 190–205, https://doi.org/10.1016/j.ijheatmasstransfer.2015.08.099.
[3] T. Gao, W.H. Zhang, J.H. Zhu, Y.J. Xu, D.H. Bassir, Topology optimization of heat conduction problem involving design-dependent heat load effect, Finite Elem. Anal. Des. 44 (14) (2008) 805–813, https://doi.org/10.1016/j.finel.2008.06.001.
[4] J. Yan, X. Guo, G. Cheng, Multi-scale concurrent material and structural design under mechanical and thermal loads, Comput. Mech. 57 (2016) 437–446, https://doi.org/10.1007/s00466-015-1255-x.
[5] L. Du, W. Hu, An overview of heat transfer enhancement methods in microchannel heat sinks, Chem. Eng. Sci. 280 (2023), https://doi.org/10.1016/j.ces.2023.119081. ISSN 0009-2509.
[6] R. Ali, A. Mahmoud, The influence of microchannel heat sink configurations on the performance of low concentrator photovoltaic systems, Appl. Energy 206 (2017) 594–611, https://doi.org/10.1016/j.apenergy.2017.08.202.
[7] D.B. Tuckerman, R.F.W. Pease, High-performance heat sinking for VLSI, IEEE Electr. Device L 2 (1981) 126–129, https://doi.org/10.1109/EDL.1981.25367.
[8] T. Dixit, I. Ghosh, Review of micro- and mini-channel heat sinks and heat exchangers for single phase fluids, Renew. Sustain. Energy Rev. 41 (2015) 1298–1311, https://doi.org/10.1016/j.rser.2014.09.024.
[9] J. Gao, Z. Hu, Q. Yang, X. Liang, H. Wu, Fluid flow and heat transfer in microchannel heat sinks: Modelling review and recent progress, Therm. Sci. Eng. Prog. 29 (2022) 101203, https://doi.org/10.1016/j.tsep.2022.101203.
[10] P. Gunnasegaran, H.A. Mohammed, N.H. Shuaib, R. Saidur, The effect of geometrical parameters on heat transfer characteristics of microchannels heat sink with different shapes, Int. Commun. Heat Mass Transfer. 37 (2010) 1078–1086, https://doi.org/10.1016/j.icheatmasstransfer.2010.06.014.
[11] Y. Sui, C.J. Teo, P.S. Lee, Y.T. Chew, C. Shu, Fluid flow and heat transfer in wavy microchannels, Int. J. Heat Mass Transf. 53 (2010) 2760–2772, https://doi.org/10.1016/j.ijheatmasstransfer.2010.02.022.
[12] W. Japar, N.A.C. Sidik, S. Mat, A comprehensive study on heat transfer enhancement in microchannel heat sink with secondary channel, Int. Commun Heat. Mass. Transfer 99 (2018) 62–81, https://doi.org/10.1016/j.icheatmasstransfer.2018.10.005.
[13] M. Di Capua, R. Escobar, A.J. Diaz, A.M. Guzman, Enhancement of the cooling capability of a high concentration photovoltaic system using microchannels with forward triangular ribs on sidewalls, Appl. Energy 226 (2018) 160–180, https://doi.org/10.1016/j.apenergy.2018.05.052.
[14] Y. Wu, C. Zhi, Z. Wang, Y. Chen, C. Wang, Q. Chen, G. Tan, T. Ming, Enhanced thermal and mechanical performance of 3D architected micro-channel heat exchangers, Heliyon 9 (2023) e13902, https://doi.org/10.1016/j.heliyon.2023.e13902.
[15] K.S.V. Paramanandam, B. Srinivasan, N.K. PVR, Thermal performance improvement in wavy microchannels using secondary channels, Int. J. Numer Method H 34 (4) (2024) 1811–1831, https://doi.org/10.1108/HFF-07-2023-0417.
[16] F. Feppon, G. Allaire, F. Bordeu, J. Cortial, C. Dapogny, Shape optimization of a coupled thermal fluid–structure problem in a level set mesh evolution framework, SeMA Journal 76 (2019) 413–458, https://doi.org/10.1007/s40324-018-00185-4.
[17] R. Zitouni, O. Ghriss, A. Fguiri, M.R. Jeday, Application of Stochastic Methods to Estimate Fouling Heat Exchanger, in: A. Mellit, L. Sbita, K. Kemih, M. Ghanes (Eds.), Proceedings of the 2nd International Conference on Green Energy Conversion System. ICGECS 2023. Green Energy and Technology, Springer, Singapore, 2024, https://doi.org/10.1007/978-981-97-6148-7_32.
[18] A. Fguiri, C. Marvillet, M.R. Jeday, Estimation of fouling resistance in a phosphoric acid/steam heat exchanger using inverse method, Appl. Therm. Eng. 192 (2021) 116935, https://doi.org/10.1016/j.applthermaleng.2021.116935.
[19] P. Coffin, K. Maute, Level set topology optimization of cooling and heating devices using a simplified convection model, Struct. Multidisc. Optim. 53 (2016) 985–1003, https://doi.org/10.1007/s00158-015-1343-8.
[20] B. Li, J. Hong, G. Liu, L. Ge, On identifying optimal heat conduction topologies from heat transfer paths analysis, Int. Commun. Heat Mass Transf. 90 (2018) 93–102, https://doi.org/10.1016/j.icheatmasstransfer.2017.11.003.
[21] R. Behrou, R. Ranjan, J.K. Guest, Adaptive topology optimization for incompressible laminar flow problems with mass flow constraints, Comput Method Appl M 346 (2019) 612–641, https://doi.org/10.1016/j.cma. 2018.11.037.
[22] M.P. Bendsoe, N. Kikuchi, Generating optimal topologies in structural design using a homogenization method, Comput. Methods. Appl. Mech. Eng. 71 (1988) 197–224, https://doi.org/10.1016/0045-7825(88)90086-2.
[23] T. Borrvall, J. Petersson, Topology optimization of fluids in Stokes flow, Int. J. Numer. Meth. Fluids 41 (2003) 77–107, https://doi.org/10.1002/fld.426.
[24] E.M. Dede, Multiphysics Topology Optimization of Heat Transfer and Fluid Flow Systems. The Proceedings of the COMSOL Conference 2009 Boston, 2009.
[25] G.H. Yoon, Topological design of heat dissipating structure with forced convective heat transfer, J. Mech. Sci. Technol. 24 (2010) 1225–1233, https://doi.org/10.1007/s12206-010-0328-1.
[26] A.A. Koga, E.C.C. Lopes, H.V. Nova, E.C.N. Silva, Development of heat sink device by using topology optimization, Int. J. Heat Mass Transfer 64 (2013) 759–772, https://doi.org/10.1016/j.ijheatmasstransfer.2013.05.007.
[27] G. Marck, M. Nemer, J.L. Harion, Topology Optimization of Heat and Mass Transfer Problems: Laminar Flow, Numer Heat Tr. B-Fund 63 (2013) 508–539, https://doi.org/10.1080/10407790.2013.772001.
[28] X. Qian, E.M. Dede, Topology optimization of a coupled thermal-fluid system under a tangential thermal gradient constraint, Struct. Multidisc. Optim. 54 (2016) 531–551, https://doi.org/10.1007/s00158-016-1421-6.
[29] X. Liu, L. Chen, M. Peng, W.T. Ji, W.Q. Tao, Topology optimization of the manifold microchannels with triple-objective functions, Numer. Heat Tr. B-Fund. 80 (5–6) (2021) 89–114, https://doi.org/10.1080/10407790.2021.1946309.
[30] Y. Sato, K. Yaji, K. Izui, T. Yamada, S. Nishiwaki, An Optimum Design Method for a Thermal-Fluid Device Incorporating Multiobjective Topology Optimization With an Adaptive Weighting Scheme, ASME J. Mech. Des. 140 (3) (March 2018) 031402, https://doi.org/10.1115/1.4038209.
[31] Y. Lv, S. Liu, Topology optimization and heat dissipation performance analysis of a micro-channel heat sink, Meccanica 53 (2018) 3693–3708, https://doi.org/10.1007/s11012-018-0918-z.
[32] X. Dong, X. Liu, Multi-objective optimal design of microchannel cooling heat sink using topology optimization method, Numer Heat Tr. A-Appl 77 (1) (2019) 90–104, https://doi.org/10.1080/10407782.2019.1682872.
[33] V. Subramaniam, T. Dbouk, J. Harion, Topology optimization of conjugate heat transfer systems: A competition between heat transfer enhancement and pressure drop reduction, Int. J. Heat Fluid Fl. 75 (2019) 165–184, https://doi.org/10.1016/j.ijheatfluidflow.2019.01.002.

[34] B. Zhang, L. Gao, Topology optimization of convective heat transfer problems for non-Newtonian fluids, Struct. Multidisc. Optim. 60 (2019) 1821–1840, https://doi.org/10.1007/s00158-019-02296-6.
[35] Y. Xia, L. Chen, J. Luo, W. Tao, Numerical investigation of microchannel heat sinks with different inlets and outlets based on topology optimization, Appl. Energ. 330 (2023) 120335, https://doi.org/10.1016/j.apenergy.2022.120335.
[36] G. Wang, D. Wang, A. Liu, T. Dbouk, P. Xu, A. Asif, Design and performance enhancement of thermal-fluid system based on topology optimization, Appl. Math Model (2023), https://doi.org/10.1016/j.apm.2022.11.031.
[37] B.S. Mekki, J. Langer, S. Lynch, Genetic Algorithm Based Topology Optimization of Heat Exchanger Fins Used in Aerospace Applications, in: Proceedings of the ASME 2019 International Mechanical Engineering Congress and Exposition. volume 8: Heat Transfer and Thermal Engineering. Salt Lake City, Utah, USA. November 11–14, 2019. V008T09A003, ASME, 2019, https://doi.org/10.1115/IMECE2019-10617.
[38] J. Wang, D. Melideo, X. Liu, U. Desideri, Comparative study on topology optimization of microchannel heat sink by using different multi-objective algorithms and objective functions, Appl. Therm. Eng. 252 (2024) 123606, https://doi.org/10.1016/j.applthermaleng.2024.123606.
[39] J. Zhao, M. Zhang, Y. Zhu, R. Cheng, X. Lin, L. Wang, Concurrent optimization of the internal flow channel, inlets, and outlets in forced convection heat sinks, Struct. Multidisc. Optim. 63 (2021) 121–136, https://doi.org/10.1007/s00158-020-02670-9.
[40] M. Yu, S. Ruan, X. Wang, Z. Li, C. Shen, Topology optimization of thermal–fluid problem using the MMC-based approach, Struct. Multidisc. Optim. 60 (2019) 151–165, https://doi.org/10.1007/s00158-019-02206-w.
[41] S. Zeng, P.S. Lee, Topology optimization of liquid-cooled microchannel heat sinks: An experimental and numerical study, Int. J. Heat Mass Tran. 142 (2019) 118401, https://doi.org/10.1016/j.ijheatmasstransfer.2019.07.051.
[42] A. Zou, R. Chuan, F. Qian, W. Zhang, Q. Wang, C. Zhao, Topology optimization for a Water-Cooled Heat Sink in Micro-electronics Based on Pareto Frontier, Appl. Therm. Eng. 207 (2022) 118128, https://doi.org/10.1016/j.applthermaleng.2022.118128.
[43] S. Qian, W. Wang, C. Ge, S. Lou, E. Miao, B. Tang, Topology optimization of fluid flow channel in cold plate for active phased array antenna, Struct. Multidisc. Optim. 57 (2018) 2223–2232, https://doi.org/10.1007/s00158-017-1852-8.
[44] L. Duan, H. Zhou, W. Xu, L. Li, X. Liu, Z. Du, H. Jiang, Design method of multiple inlet/outlet air cooling frame of pouch lithium-ion battery based on thermal-fluid coupling topology optimization, Int. J. Heat Mass Tran. 215 (2023) 124496, https://doi.org/10.1016/j.ijheatmasstransfer.2023.124496.
[45] H. Li, X. Ding, F. Meng, D. Jing, M. Xiong, Optimal design and thermal modelling for liquid-cooled heat sink based on multi-objective topology optimization: An experimental and numerical study, Int J. Heat Mass Tran. 144 (2019) 118638, https://doi.org/10.1016/j.ijheatmasstransfer.2019.118638.
[46] X. Chen, X. Xu, M. Li, Y. Li, H. Ling, Multi-objective topology optimization design of silicon carbide metal oxide semiconductor field effect transistors power module liquid-cooled heatsink for electric vehicles, Appl. Therm. Eng. 254 (2024) 123861, https://doi.org/10.1016/j.applthermaleng.2024.123861.
[47] D. Wang, Q. Wu, G. Wang, H. Zhang, H. Yuan, Experimental and numerical study of plate heat exchanger based on topology optimization, Int. J. Therm. Sci. 195 (2024) 108659, https://doi.org/10.1016/j.ijthermalsci.2023.108659.
[48] N. Pollini, O. Sigmund, C. Andreasen, J. Alexandersen, A "poor man's" approach for high-resolution three-dimensional topology optimization of natural convection problems, Adv. Eng. Softw. 140 (2020) 102736, https://doi.org/10.1016/j.advengsoft.2019.102736.
[49] A. Ghasemi, A. Elham, Multi-objective topology optimization of pin-fin heat exchangers using spectral and finite-element methods, Struct. Multidisc. Optim. 64 (2021) 2075–2095, https://doi.org/10.1007/s00158-021-02964-6.
[50] J. Zhao, M. Zhang, Y. Zhu, R. Cheng, L. Wang, Topology optimization of planar cooling channels using a three-layer thermofluid model in fully developed laminar flow problems, Struct. Multidisc. Optim. 63 (2021) 2789–2809, https://doi.org/10.1007/s00158-021-02842-1.
[51] G. Marinaro, A. Fragnito, G.M. Mauro, E. Frosina, A. Pagano, N. Bianco, Heat sink design and topology optimization of a DC/AC converter for a general aviation hybrid-electric aircraft, Appl. Therm. Eng. 258 (Part B) (2025) 124663, https://doi.org/10.1016/j.applthermaleng.2024.124663.
[52] S. Sun, P. Liebersbac, X. Qian, Large Scale 3D Topology Optimization of Conjugate Heat Transfer, in: 2019 18th IEEE Intersociety Conference on Thermal and Thermomechanical Phenomena in Electronic Systems (ITherm), Las Vegas, NV, USA, 2019, pp. 1–6, https://doi.org/10.1109/ITHERM.2019.8757230.
[53] B. Rogié, C.S. Andreasen, Design complexity tradeoffs in topology optimization of forced convection laminar flow heat sinks, Struct. Multidisc. Optim. 66 (2023) 6, https://doi.org/10.1007/s00158-022-03449-w.
[54] T. Zhang, X. Yang, X. Wang, Level set-based topology optimization for thermal-fluid system based on the radial basis functions, Appl. Math. Model. 113 (2022), https://doi.org/10.1016/j.apm.2022.09.005.
[55] E.M. Dede, Optimization and Design of a Multipass Branching Microchannel Heat Sink for Electronics Cooling, ASME J. Electron. Packag. 134 (4) (December 2012) 041001, https://doi.org/10.1115/1.4007159.
[56] Y. Zhou, T. Nomura, E.M. Dede, Topology Optimization of Manifold Microchannel Heat Sinks, in: 2020 19th IEEE Intersociety Conference on Thermal and Thermomechanical Phenomena in Electronic Systems (ITherm), Orlando, FL, USA, 2020, pp. 740–746, https://doi.org/10.1109/ITherm45881.2020.9190257.
[57] N. Gilmore, V. Timchenko, C. Menictas, Manifold microchannel heat sink topology optimisation, Int. J. Heat Mass Transf. 170 (2021) 121025, https://doi.org/10.1016/j.ijheatmasstransfer.2021.121025.
[58] D. Yu, M. Rachik, A. Blaise, B. Sarre, G. Brun, Topology optimization designed twisted conformal cooling channel for additive-manufactured hot-stamping tool, Appl. Therm. Eng. 124784 (2024), https://doi.org/10.1016/j.applthermaleng.2024.124784.
[59] K. Svanberg, The method of moving asymptotes—a new method for structural optimization, Int. J. Numer Meth. Eng. 24 (1987) 359–373, https://doi.org/10.1002/nme.1620240207.
[60] K. Svanberg, A Class of Globally Convergent Optimization Methods Based on Conservative Convex Separable Approximations, Siam J. Optimiz. 12 (2) (2002) 555–573, https://doi.org/10.1137/S1052623499362822.
[61] B.S. Lazarov, O. Sigmund, Filters in topology optimization based on Helmholtz-type differential equations, Int. J. Numer. Meth. Eng. 86 (2011) 765–781.
[62] J. Donea, A. Huerta, Finite element methods for flow problems, John Wiley & Sons, 2003.
[63] Y. Deng, T. Zhou, Z. Liu, S. Qian, Y. Wu, J.G. Korvink, Topology optimization of electrode patterns for electroosmotic micromixer, Int. J. Heat. Mass. Tran. 126 (2018) 1299–1315.
[64] F. Tröltzsch, Optimal Control of Partial Differential Equations: Theory, Methods, and Applications, Vol. 112, American Mathematical Soc, 2010.
[65] M. Hinze, R. Pinnau, M. Ulbrich, S. Ulbrich, Optimization with PDE Constraints, Springer, 2009.
[66] S. Qian, S. Lou, C. Ge, W. Wang, X. Tian, Y. Cai, The influence of temperature dependent fluid properties on topology optimization of conjugate heat transfer, Int. J. Therm. Sci. 173 (2022) 107424, https://doi.org/10.1016/j.ijthermalsci.2021.107424.
[67] P. Huang, M. Pan, Secondary heat transfer enhancement design of variable cross-section microchannels based on entransy analysis, Renew. Sust. Energ. Rev. 141 (2021) 110834, https://doi.org/10.1016/j.rser.2021.110834. ISSN 1364-0321.